We appreciate all the great efforts and constructive comments from the reviewers. We have revised the manuscript carefully according to the reviewers' comments and suggestions. Our point-by-point responses and changes are appended below in blue fonts.

Anonymous Referee #1

Received and published: 26 June 2019

Summary:

This manuscript presents observations of persistent gravity wave activity in a stable atmospheric boundary taken as part of a field experiment over Anqinq, China. Alongside the observations, a series of CFD simulations are conducted in order to understand the likely mechanisms for generation of these gravity waves. The results are not particularly novel – gravity waves have been observed in previous studies of the ABL and shear is known to be an important mechanism for generation of gravity waves. Having said that, the observations make a nice case study, bringing together Doppler lidar observations with some radiosonde data to give an unusually detailed set of observations of such waves.

Response: Thanks a lot for your comments. Although GWs in ABL have been observed in previous studies and shear is known to be an important mechanism. GWs from surface to ~2 km with long lifetime more than 10 hours and 20 wave cycles are reported rarely. Both observations and simulations are used to analyze this unique GW activity. Therefore, we believe that this study of long-lived GWs in ABL is novel and interesting to the readers.

Major comments:

1) The general motivation for the work is perhaps a little misleading. The introduction talks about the breaking of gravity waves at critical layers at altitude and the role of high frequency waves in momentum transport into the upper troposphere. The observations presented are of vertically coherent waves which look much more like horizontally propagating trapped wave modes to me, and hence it is not clear the relevance of either of these? Such horizontal modes might well be important and linked to low level turbulence (e.g. the role of trapped waves in generation of rotors as in the T-Rex experiment, Grubisic et al, 2008) and they have also been linked to the initiation of convection (e.g. Lac et al, 2002; Marsham

and Parker, 2006; Birch et al, 2012). You might also mention low level wave drag (e.g. Lapworth and Osborne, 2016; Tsiringakis et al, 2017).

Response: Thanks for this suggestion. The introduction is rewritten according to your suggestion to emphasize the motivation of this study.

Changes: Page 1, line 31 to page 2, line 8. "In general, most of these GWs will propagate upward into the upper atmosphere, e.g. upper troposphere, stratosphere, mesosphere and even thermosphere. Leading to transportation of energy and momentum from lower atmosphere to upper atmosphere, and thus affect the coupling between lower atmosphere and upper atmosphere, as well as dynamic and thermal structure of the global atmosphere (Fritts and Alexander, 2003; Holton and Alexander, 2000). However, trapped GWs, e.g. trapped lee waves and ducted motions with high frequency and coherent variability, could only propagate horizontally. In the lower atmosphere, these horizontally propagating GWs may be linked to low level turbulence (e.g. rotors), the initiation of convection and low level wave drag (Birch et al., 2013; Grubišić et al., 2008; Lac et al., 2002; Lapworth and Osborne, 2016; Marsham and Parker, 2006; Tsiringakis et al., 2017). Therefore, such trapped GWs play a key role in weather forecast, climate models and aviation safety."

The introduction also suggests (page 1, line 29) that waves are only generated in the troposphere, which is not true.

Response: The GWs are usually generated in the troposphere in the introduction (page 1, line 29), not only generated in the troposphere.

It is also not clear what the specific motivation for this work is. How might this work help to i) deepen our understanding of the mechanism leading to the generation and propagation of gravity waves in the boundary layer and/or ii) improve our capability to model these waves or parametrise their effects? How might the results be useful to researchers in other regions of the world? You probably want to return to these questions in the conclusions and discussion.

Response: In the 3rd paragraph of Introduction, we have mentioned that most of the observed ducted waves in the ABL are limited to the surface layer within tens or hundreds of meter near ground in previous studies. GWs from surface to ~2 km with long lifetime more than 10 hours and 20 wave cycles are rarely reported. Compared to previous studies, this work will make contribution to deepen and enhance our understanding of such unique long-lived ducted GWs.

Changes: Page 14, line 25 to line 31. “The wave motions mentioned above were mainly observed in the stable boundary layer under the height of ~1000 m or even ~100 m, while the wave motions exist from surface layer to as high as ~2000 m in our study due to different capability of measurements. In addition, the lifetime of the ducted GWs is more than 10 hours and 20 wave cycles, while in previous studies listed above, most of the lifetimes are less than hours with several wave cycles. These characters make this ducted GWs unique and novel. However, in one of our previous study, obvious wave motions with periods of 10~30 min in vertical wind were observed in the whole residual layer from 1 June 2018 to 2 June 2018 by a similar CDL system (Wang et al., 2019).”

2) It would be useful to the reader, and increase the impact of your work, if you can highlight the novelty of this work given that various other studies have observed and modelled gravity waves in the boundary layer, including many of the papers referenced in the introduction.

Response: Thanks for this suggestion. To the best of our knowledge, other reported observations of such ducted GWs are generally trapped within tens or hundreds of meter near ground and short time over few hours. We have mentioned this in the Introduction and Discussion. To study the GWs, we built a robust and mobile coherent Doppler wind lidar with good detection capability. In the field experiment, continuous wind observation of the GWs are captured to a height about 2000 m over a lifetime of tens hours. This rarely observed case provides us an opportunity to study such GWs.

Changes: Page 14, line 25 to line 31. “The wave motions mentioned above were mainly observed in the stable boundary layer under the height of ~1000 m or even ~100 m, while the wave motions exist from surface layer to as high as ~2000 m in our study due to different capability of measurements. In addition, the lifetime of the ducted GWs is more than 10 hours and 20 wave cycles, while in previous studies listed above, most of the lifetimes are less than hours with several wave cycles. These characters make this ducted GWs unique and novel. However, in one of our previous study, obvious wave motions with periods of 10~30 min in vertical wind were observed in the whole residual layer from 1 June 2018 to 2 June 2018 by a similar CDL system (Wang et al., 2019).”

3) Table 1 gives the spatial resolution. I assume this is the along-beam range gate size? It would be useful to clarify this. There are two additional factors to consider. Firstly, the beam spread angle will alter the effective horizontal resolution of each sample (increasing with height). Perhaps more importantly the Doppler wind retrieval requires multiple scans (1 vertical and at least 2 at an angle – here 30◦). This means the wind retrieval is over a cone with a much larger width than the 60m resolution given. At 2km the radius of this cone would be 1150m. This might be a significant fraction of the wavelength of a short, high frequency wave. These issues should at least be discussed.

Response: Thanks for this suggestion. These issues are added in Discussions in the revised manuscript. The retrieval of the horizontal wind is based on the hypothesis of a homogeneity wind field on a horizontal plane. Accompanying with wave activities, the radius of the cone will lead to some bias on the horizontal wind if the radius is equivalently to or larger than the scale of the waves. Nevertheless, the effect on the period of the wave motions is negligible. If the radius is smaller than the scale of waves significantly, these bias can be also ignored.

Changes: Page 16, line 3 to line 10. "It should be noted that the retrieval of horizontal wind is based on the hypothesis of a homogeneity wind field on a horizontal plane. Accompanying with wave activities, the radius of scanning beams cone will lead to bias on the retrieved horizontal wind. If the radius is equivalently to or larger than the scale of the horizontal wavelength of the GWs, these bias may be significantly affect the result in horizontal component, especially the amplitude of the retrieved GWs. Nevertheless, the bias in the period of the wave motions is negligible. If the radius is smaller than the scale of the horizontal wavelength of the GWs, the bias in both amplitude and period can be ignored. In this study, the horizontal wavelength is estimated as ~3 km in Sect. 4.2. The radius is about 580 m and 870 m at 1 km and 2 km altitude, respectively. Thus, the retrieved bias can be ignored in this study."

4) Bottom of page 4. These jets are important as the shear associated with them is hypothesised to lead to the gravity waves. It is not clear what the cause of these jets is though. The big changes in wind direction are unusual. Can you offer any explanation? It is possible that the upper jet is some sort of nocturnal low level jet as it seems to strengthen during the night and weaken a little around dawn, but there is not much

evidence of wind turning with time as one might expect to see if this was an inertial oscillation. Have you tried looking at hodographs at a specific height from the lidar winds to see evidence of this? Are there other explanations, e.g. the height of the surrounding topography leading to channelling in the valley?

Response: Thanks. During the field experiments, it seems that most of these jets are nocturnal low level jet from Fig. A2-3. The changes in wind direction of ~90 °are not unusual in Fig. A3. It is difficult to see if this was an inertial oscillation with a change in wind direction of ~90 ° for us. The surrounding topography, e.g., Dabie Mountain and Mountains around Huangshan, and weather system, e.g., Typhoon passed by, may have an effect on this change in wind direction. However, these question are beyond our scope of this study. If someone is interested in this subject, future studies of these jets and cooperation may be helpful after the peer-review completion.

5) Page 6, line 2. It seems likely that this aerosol concentration profile is associated with a stably stratified boundary layer, but I'm not sure that you can definitively say this from the lidar observations since you have no direct measure of temperature or stability.

Response: Thanks. We changed this description in the revised manuscript.

Changes: Page 6, line 2 to line 3. "Thus the ABL seems to be stably stratified as the CNR may represents the aerosol concentration in some cases."

6) Page 7, figure 5. It would be useful to include a plot of the Scorer parameter here in addition to N2 since it is hypothesised that wind shear is important.

Response: Thanks for this suggestion. In Fig. 10, we have plot the vertical profile of vertical wave number squared, which is also associated with wind shear as shown in Taylor-Goldstein equation (Eq. 4). The Scorer parameter l is given by the following equation:

$$l^2 = \frac{N^2}{U^2} + \frac{\bar{u}_{zz}}{U} \qquad \text{(R1)}$$

where U is the vertical profile of the barrier normal component of the horizontal wind, and other parameters are defined in the manuscript. The dominant first two terms on the right-hand side in Eq. 4 are similar to those two terms on the right-hand side in Eq. R1, except that intrinsic phase speed c_i is replaced by horizontal wind speed U. The role of wind shear has been discussed in the Discussion with the Taylor-Goldstein equation.

7) Page 7, lines 17-18. I am not sure you can say anything about the presence of absence of waves above 1800-2000m. The lidar barely extends above 2000m between 0400-0900 and the CNR is quite low, with noisy w fields. I would reword this conclusion.

Response: Thanks. We delete this description in the revised manuscript.

8) Page 8, Figure 6. If you are plotting W1 and W2 in the text, then you need to at least briefly explain them here. The main text should be understandable without reading the appendix. The appendix is for additional details. At the moment the figure is meaningless without knowing what it means having only W1 or only W2. (Actually this is still not very clear, even after reading the appendix – see below).

Response: Thanks. We are regret for the missing description of W1 and W2 here in the manuscript. W1 and W2 are the potential waves identified by LS spectral and Morlet wavelet spectral, respectively. Only W1 (W2) means the potential waves are only identified by LS (Morlet wavelet) spectral method, and not identified by Morlet wavelet (LS) spectral method, simultaneously.

During the revision, we reconsidered this part of GW identification. We present this part to demonstrate the relation between GW occurrences and background wind. However, on the one hand, this relation has been studied in several previous studies (Mahrt, 2014) and can be also analyzed in Sect. 4.2. On the other hand, the method if GW identification described in Appendix B is simple and rough, not serious as discussed in Appendix B. Therefore, we decided to delete these text and figure related to GW identification during the whole field campaign in the revised manuscript. The same to the Appendix B. This deletion will not affect the analysis and result of this work. At the same time, this deletion will also help us concentrate on the analysis of the unique long-lived ducted GW.

Changes: Appendix B is deleted. Sect. 3.2 is reorganized as follows:

"There are complex relationships between GWs and background wind conditions. Submeso wavelike motions, that any nonturbulent motions on horizontal scales smaller than 2 km and with periods of tens of minutes, are primarily generated in very weak winds in nocturnal boundary layer (Mahrt, 2014). Noted that the wind speed from 4 to 5 in September 2018 are weakest during the whole field experiment in Fig. A2. In order to understand the relationship between this ducted GW and background wind, a temporal spatial window of 1-hour length and 200-m height, and shifted in steps of 1 hour temporally and 100 m vertically is used. Mean horizontal wind speed and wind direction in each window during the whole field campaign in Anqing are easily obtained.

The wind rose of the horizontal wind during the field experiment is shown in Fig. 6. It is apparent that northeasterly wind and southwesterly wind are prevailing around the station in the ABL during the whole field campaign. The infrequently observed ducted GWs in Fig. 2 occur accompanying infrequently westerly weak wind. It is interesting to note that the long-narrow plain area along Yangtze River around Anqing between Huangshan and Dabie Mountain is also along the direction of northeast-southwest as shown in Fig. 1a. The typical elevations of Huangshan and Dabie Mountain are about 1~2 km. Strong wind along northwest-southeast direction may be blocked in the ABL, thus leading to the weak wind along northwest-southeast direction after the wind flowing over Huangshan or Dabie Mountain and the prevailing wind along northeast-southwest direction. As GWs are favour to generate in weak wind conditions. we can imagine that Dabie Mountain and Huangshan may have an impact on GWs in Anqing. However, surrounding hills around the station as shown in Fig. 1b may also affect the generation and existence of GWs. The effect of surrounding hills will be studied by numerical simulations in next section."

9) Page 8, Figure 6. Also, are these plots for the whole field campaign or just the case study on 4th - 5th Sept. What height did you go up to? How was this chosen?

Response: These plots are for the whole field campaign in Anqing. The height range is from 100 m to 2000 m above ground. In the raw manuscript, a temporal spatial window of 4-hour length and 200-m height, and shifted in steps of 1 hour temporally and 100 m vertically is employed. The window is utilized only when valid data covers greater than 80% of the window. In this condition, GWs can be roughly identified with the method described in Appendix B. Therefore, the height is decided by the carrier to noise ratio (CNR) of the raw data. As responded in major comment 8, Fig. 6 and related text are deleted to concentrate on the analysis of the unique long-lived ducted GW.

Changes: Page 8, line 8 to line 9. “Mean horizontal wind speed and wind direction in each window during the whole field campaign in Anqing are easily obtained.”

10) Page 9, lines 15-16. This is a very bold claim! Both the terms "mesoscale models" and "CFD models" can cover a wide range of different things. Ultimately both are solving the same equations. Which is better will depend on the details of individual models and their numerics, and the setup of individual simulations (e.g. resolution, turbulence scheme etc.). CFD models traditionally do not include many atmospheric processes, although the distinction is increasingly blurred. All your advantages could equally apply to a high resolution atmospheric model. I would just remove this sentence altogether.

Response: We agree that both mesoscale models and CFD models are solving the same equations. The mesoscale numerical model considers the multi-physical process (e.g., wind, temperature, humidity, water vapor). However, mesoscale model seams too coarse for analyzing microscopic terrain**.** In contrast, the CFD model makes up for the inadequacies of mesoscale with high resolution. In addition, CFD mode has the ability to capture micro turbulence structures. Most mesoscale models have coarser net grids than CFD models employed in this work. We delete this sentence in the revised manuscript.

11) Page 9, section 4.1. So which CFD model are you actually using? Is this a commercial code? Include a reference to the actual model and its validation if at all possible.

Response: The Renormalization group k-epsilon (RNG k-ε) model is employed in this work, which is proposed by (Yakhot et al., 1992). A more comprehensive description of RNG k-ε theory and its application to turbulence can be found in (Orszag, 1993). The RNG k-ε models products reliable predictions for wind flows over hilly terrain (Kim et al., 2000), are more computationally efficient than the Large Eddy Simulation (LES) models. The RNG k-ε model is a quite mature model which is widely verified in simulation of wind flow over complex terrain in recent years (El Kasmi and Masson, 2010; Yan et al., 2015).

The RNG k-ε turbulence model based on OpenFOAM is used in this work. OpenFOAM is the leading free, open source software for computational fluid dynamics (CFD), owned by the OpenFOAM Foundation and distributed exclusively under the General Public Licence (GPL). The GPL gives users the freedom to modify and redistribute the software and a guarantee of continued free use, within the terms of the licence. Open-source CFD tool is a more powerful research tool in comparison to proprietary software because of its flexibility to incorporate new implementation of field calculation and post-processing, attracts users from both industry and academia. The details of the RNG k-ε model and core codes can be found in the following website: https://www.openfoam.com/documentation/guides/latest/api/classFoam_1_1RASModels_1_1RNGkEpsilon.html.

Changes: Page 9, line 14 to 19. "In this study, a two-equation RANS model based on renormalisation group (RNG) methods is used to simulate wind field. The RNG k-ε model was developed to renormalize the Navier-Stokes equations which are account for the effects of smaller scale motions (Yakhot et al., 1992). The RNG k-ε model is a quite mature model which is widely verified in simulation of wind flow over complex terrain in recent years (El Kasmi and Masson, 2010; Yan et al., 2015). The RNG k-ε turbulence model used in this work is based on OpenFOAM. OpenFOAM is the leading free, open source software for CFD simulations."

12) Page 10, lines 13-14. With the first cell height at 5m then you are not resolving the roughness sub-layer at all, and so you need to apply some sort of wall function / Monin-Obukov similarity function rather than just the no-slip boundary condition. Are you doing this? If so, what?

Response: For a fully rough surface the roughness length z_0 and the roughness height k_s are related via $k_s = z_0 e^{KB}$, where K is the von Karman constant (K≈0.4) and B≈8.5 is the constant in the logarithmic velocity profile for rough surfaces (Franke et al., 2004). z_0 is set as 0.15 for the landforms in this paper. After grid independence verification, the first layer height is 5.0 m for considering a wall function, when the resolution of the terrain is 20 m. A good result was obtained with almost the same mesh set as in this study, indicating that the present mesh generation is reasonable (Ren et al., 2018).

A rough-wall function was adopted, of which the formula is as follows (Ren et al., 2018):

$$\frac{u}{u^*} = \frac{1}{K} In(\frac{Ez_c}{Ck_s}) \quad \text{(R2)}$$

where E=9.793 is the wall constant, C = 0.327 is a roughness constant, z_c is the distance to the cell center of the first wall adjacent cell, u is the velocity in the cell center, u^* is the friction velocity.

Changes: Page 10, line 5 to 9. “A rough-wall function is adopted, of which the formula is as follows (Ren et al., 2018):

$$\frac{\mathrm{u}}{\mathrm{u}^{*}} = \frac{1}{\mathrm{K}}\mathrm{In}\left(\frac{\mathrm{Ez_c}}{\mathrm{Ck_s}}\right) \tag{4}$$

where E=9.793 is the wall constant, C = 0.327 is a roughness constant, K≈0.4 is the von Karman constant, k_s is the roughness height, z_c is the distance to the cell center of the first wall adjacent cell, u is the velocity in the cell center, u^* is the friction velocity.”

13) Presumably there is a prognostic equation for potential temperature or similar, in order to include stability effects? No mention of this. What boundary conditions are used for this variable?

Response: The CFD cases conducted in this study are used to reveal the influence of topography and wind shear on the generation of the persistent GWs. The thermal field is assumed to be uniform on horizontal direction. Temperature profiles from radiosonde on 5 September is applied in this model. For this ducted GWs, buoyant flows are developed with low velocity and small temperature variations. As a result, the Boussinesq model is used in study, which considers only the effect of buoyancy in gravity terms. The Boussinesq approximation can be used instead of a constant density. This model treats density as a constant value ρ_{ref} in all solved equations, except for the gravity and buoyancy term. The density is approximated as:

$$\rho = \rho_{ref} - \rho_{ref}\beta(T - T_{ref}) \tag{R3}$$

where β is the thermal expansivity, T_{ref} is a reference temperature. the couple of thermal and velocity is realized by air density which the function with temperature.

Changes: Page 10, line 15 to 18. “The CFD cases conducted in this study are used to reveal the influence of topography and wind shear on the generation of the persistent GWs. The thermal field is assumed to be uniform in a horizontal plane. Temperature profile from radiosonde on 5 September is applied in this model. In this work, buoyant flows are developed with low velocity and small temperature variations. As a result, the Boussinesq model is used in this work, which considers only the effect of buoyancy in gravity terms. The Boussinesq approximation can be used instead of a constant density. This model treats density as a constant value ρ_{ref} in all solved equations, except for the gravity and buoyancy term in the momentum equation. The density ρ is approximated as:

$$\rho = \rho_{ref} - \rho_{ref}\beta(T - T_{ref}) \quad (5)$$

where β is the thermal expansivity, T_{ref} is a reference temperature."

14) Page 10, line 9. What do you mean by "symmetric condition" at the upper interface? Which variables does this apply to?

Response: The actual conditions of upper interface are difficult to obtain. The upper interface of the computational domain are external boundaries representing the far fields of flow. If a constant pressure is applied in these boundaries, this may alter the inlet wind profile in case the prescribed pressure is not matched with the boundary velocity (Luketa-Hanlin et al., 2007). Symmetry condition can be used at the top boundaries to reserve the wind profile and eliminate the effect of changing the inlet profiles. On this condition, zero Gradient is set for all vertical physical variables, and the vertical velocity is set as zero (Tran et al., 2019). In addition, symmetric condition facilitates computational convergence. Therefore, the upper interface is assumed as symmetric condition, which facilitates computational convergence.

Changes: Page 9, line 31 to page 10, line 1. "On this condition, zero gradient is set for all vertical physical variables, and the vertical velocity is set as zero."

15) Page 11, lines 17-18. I don't understand the comment that the flow solution is initiated as a steady state in all cases except case 7 and 8. How can you initiate at a steady state? Do you mean you initialise with the merged wind profile everywhere? In general this will not be an exact solution to the model equations, even in 1-d, so this isn't a steady state. Even if it was a solution in 1-d, the inclusion of topography means there will be variations across the domain which you cannot know without solving first. I assume the additional complication for cases 7 and 8 is that the addition of a constant velocity everywhere would break the no-slip boundary condition. How do you deal with that? Is the velocity near the surface reduced to produce a consistent initialisation / inlet profile? If so, how?

Response: We do not mean initialise with the merged wind profile everywhere. The initial wind profile everywhere is set to be zero, except inlet. The steady state means the state when the turbulence developed fully, i.e., when the wind-inlet passed by the ABL and varies regularly above lidar station. The inlet profile is consistent. In case 7 and 8, the turbulences do not develop fully until the time of ~2 hour and ~1 hour, respectively. After that time in case 7 and 8, and after time of 0 in all other cases, the flow dynamics vary regularly as shown in Fig. 9 in raw manuscript.

Changes: Page 11, line 10 to line 14. “It should be noted that the time of 0 represents a steady state in all cases except case 7 and 8. Here, the steady state means the state when the turbulence developed fully, i.e., when the wind-inlet passed by the ABL and varies regularly above lidar station. In case 7 and case 8, the time of 0 is defined as when the simulations started running and the velocity-inlet flowed from the west boundary at the same time.”

16) Page 11, table 2. You don’t actually define u0. I assume this is the merged wind profile (lines 4-6), in which case define it there. It would be useful to have a plot of this model wind profile, and also the potential temperature profile.

Response: Yes, u_0 is the merged wind. This has been pointed in the revised manuscript.

Changes: Page 10, line 24 to line 25. “The 1-hour mean zonal wind under 2 km from lidar and zonal wind above 2 km from ERA5 reanalysis data at 00:00 in 5 September 2018 are merged as the sustained import wind profile u_0 in the west boundary of the computational domain.”

17) The simulations presented are all 2-D, however the analysis elsewhere suggests that topography might be constraining the low level flow. Why choose to conduct 2-D simulations? What is the impact of this? This choice needs to be justified, and the limitations discussed.

Response: When simulating wind flow in complex mountain areas, more accurate results can be obtained by using 3D model with accurate boundary conditions. However, the actual wind field and terrain are complex. It is difficult to obtain accuracy boundary conditions for 3D model. In addition, 3D model consumes much more computing resources and time than 2D model.

As a simplification of the actual mountain model, the comparison between numerical simulation results and field experiments shows that the two-dimensional model can simulate the actual topographic flow well (Miller and Davenport, 1998; Toparlar et al., 2017; Walmsley et al., 1984). Some basic theories and empirical formulas of complex mountain wind field are built on the basis of two-dimensional model. Therefore, the two-dimensional terrain simulation of mountain wind field has a wide range of theoretical significance and practicability.

Changes: Page 16, line 11 to line 19. "More accurate results can be obtained by using three-dimensional (3D) model with accurate boundary conditions when simulating wind flow in complex mountain areas. However, the actual wind field and terrain are complex. It is difficult to obtain accuracy boundary conditions for 3D model. In addition, 3D model consumes much more computing resources and time than 2D model. As a simplification of the actual mountain model, the comparison between numerical simulation results and field experiments shows that the two-dimensional model can simulate the actual topographic flow well (Miller and Davenport, 1998; Toparlar et al., 2017; Walmsley et al., 1984). Some basic theories and empirical formulas of complex mountain wind field are built on the basis of two-dimensional model. Therefore, the two-dimensional terrain simulation of mountain wind field has a wide range of theoretical significance and practicability. By using this simplified 2D model, the influence of terrain on GWs can be still analyzed."

18) Page 13, lines 15-16. If these waves were topographically generated, one would expect stationary waves rather than the propagating waves seen here. You have only shown time-height plots. If you look at vertical cross sections is there evidence of stationary topographically generated gravity waves at all?

Response: We have shown cross sections of vertical wind and zonal wind in the whole 2-D simulation domain in the video supplement (https://doi.org/10.5446/41847). In this movie, some quasi-stationary topographically generated GWs can be found around the east (right) hill.

19) While there are a relatively comprehensive set of simulations presented here, there is relatively little attempt to explain physically why the differences between the simulations occur. It might be fruitful to look at the Scorer parameter for different wind profiles. Does this explain the differences in wave trapping observed for example? One factor which is not investigated at all is the role of stability. Without stability there would be no waves at all, and the presence of these trapped horizontal wave modes must be at least partly due to the low level inversion. How would altering this affect the results?

Response: The temperature profiles are the same among the 16 cases. The stabilities will only vary with vertical profiles of horizontal wind in Scorer parameter as shown in Eq. R1. We agree that partly of the trapped horizontal wave modes due to the inversion layer, which has been discussed in Fig. 10 in raw manuscript. "The thermal duct is dominant under the temperature inversion with maxima buoyancy frequency squared for all propagation directions as shown in Fig. 5. The Doppler duct is dominant between ~0.5 and ~1.5 km altitude range due to the critical level induced by the low-level jet of wind maximum in a particular direction."

20) Page 13, line 22. It is rather unusual to see negative values of N at 2km. This implies an unstable atmosphere at this height. Do you have any idea what is driving this? I note that these negative values are fairly small, and only over a narrow height range (Figure 5b). It is interesting to note that the waves appear to reach well above the stable boundary layer in this case (perhaps 200-300m depth), even though there are several near-neutral levels below 2km. Can you explain this? Plotting temperature profiles (rather than potential temperature) and the choice of scales for the N2 plot makes this difficult to judge though.

Response: The negative values of N^2 may be due to the rapid decrease of temperature with altitude as shown in Fig. 5a. This may be relation to the ABL top. The temperature, water vapor and aerosols are mixed better under this top due to stronger turbulence than above this top. It is a result of the combination of thermal (stable boundary layer) and Doppler ducts. The Doppler duct play a dominant role above the stable boundary layer as discussed in the Discussion. Potential temperature profiles are added in the revised Fig. 5.

21) Appendix B. From what is written I cannot see why you need to choose and compare two separate wave frequencies W1 and W2. From figure B1 I am guessing that W1 is the most significant peak with LS and W2 the most significant peak with the Morlet wavelet? The text does not explicitly say this. Similar, I am assuming from the figure that the wave is identified as the most significant peak, although this is not explicitly stated. Only when similar waves are identified by both methods is the case treat as a GW. Why do you use this criterion? This whole section could be better explained.

Response: Yes, the most significant wave is identified by compare W1 and W2. If a wave is significant in a temporal window, this wave can be identified by different method. Some turbulence or noise may be treated as waves with only one method. However, this method is simple and rough, not serious. As responded in major comment 8, we deleted this section and related part in the text in the revised manuscript in order to avoid confusing readers.

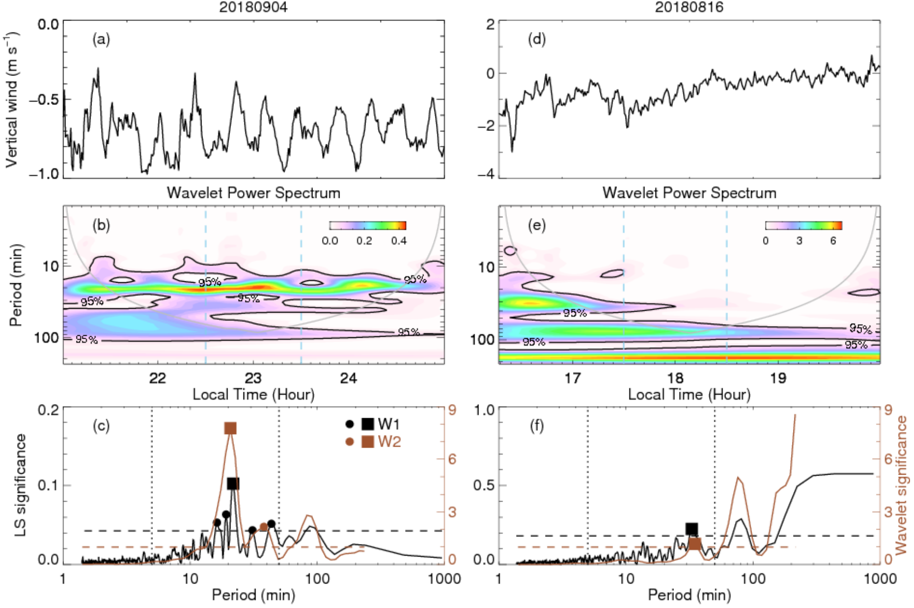

Figure R1. The same to Fig. B1 in the raw manuscript. But (d-f) are replaced by false detection.

22) Page 22, line 1. Do you have any evidence of false detection? Are any of the wave signals unrealistic? There doesn’t seem much evidence to confirm or deny this at the moment so it is rather speculative.

Response: Yes, we have. A false detection is shown in Fig. R1d-f. Though with some false detection, we thought the statistical results are still useful to enrich our knowledge of such waves as discussed in second paragraph in Appendix B. As responded in major comment 8, we deleted this section and related part in the revised manuscript.

References

Birch et al (2013) Impact of soil moisture and convectively generated waves on the initiation of a West African mesoscale convective system. QJRMS 139 1712-1730.

Grubisic et al (2008) THE TERRAIN-INDUCED ROTOR EXPERIMENT: A Field Campaign Overview Including Observational Highlights. BAMS 89 1513–1534.

Lac, Lafore and Redelsperger (2002) Role of Gravity Waves in Triggering Deep Convection during TOGA COARE. JAS 59 1293–1316.

Lapworth and Osborne (2016) Evidence for gravity wave drag in the boundary layer of a numerical forecast model: A comparison with observations. QJRMS 142 3257–3264.

Marsham and Parker (2006) Secondary initiation of multiple bands of cumulonimbus over southern Britain. II: Dynamics of secondary initiation. QJRMS 132 1053-1072.

Tsiringakis, Steenveld, Holtsag (2017) Small-scale orographic gravity wave drag in stable boundary layers and its impact on synoptic systems and near-surface meteorology. QJRMS 143 1504–1516.

Minor comments:

Title. “Long-lived High Frequency Gravity Waves in the Atmospheric Boundary Layer”
would be better English.

Response: Changed as suggested.

Page 4, line 4. “Wind field”

Response: Corrected.

Page 4, line 20. “4-dimensions”

Response: Corrected.

Page 6, Fig 3 caption. Should this be “Cone-of-Influence”?

Response: Corrected.

Page 7, line 15. Units should not be in italics.

Response: Corrected.

Page 9, line 2. The word “quadrature” is not really appropriate here. I would say “is perpendicular to the corresponding wind rose”. This occurs at other places in the text too.

Response: Corrected.

Page 9, line 25. “simulate the wind field”.

Response: Corrected.

Page 12, figure 9 caption. “wave motions are not only exist in the vertical wind”. “no wave motions are generated”. “cases 2-4”

Response: Corrected as suggested.

Page 15, line 18. “. . . perturbations of the GW were 90◦ out of phase with vertical perturbations...”

Response: Corrected as suggested.

Anonymous Referee #2

Received and published: 13 August 2019

The manuscript presents the results of lidar observations of wave like variations of wind velocity vector vertical and horizontal components in the boundary layer of atmosphere obtained during the field experiment in August-September 2018 in the location of Anqing, China. The experimental results are accompanied by the results of model numerical simulation of the wind field disturbed by the topographical objects. Based on the obtained experimental and computational results the conclusions about mechanism of generation of wave variations of wind velocity are formulated in the manuscript.

Major comments:

1) The general goal of the study is not clear from the manuscript. It may be proposed that this goal is study of atmospheric waves arising under conditions of stable thermal stratification in the boundary layer of atmosphere. But only one event of atmospheric wave on 4-5 September is analyzed in the manuscript with the use of information about the profile of temperature in height. Moreover, even for that event there is no data on temperature profile measured with the radiozonde at 19:15 on 4th September in the manuscript. To improve understanding of this issue, it may be useful to present the temperature profiles in height during all the period of field experiment and carry out the analysis of frequency of wave events

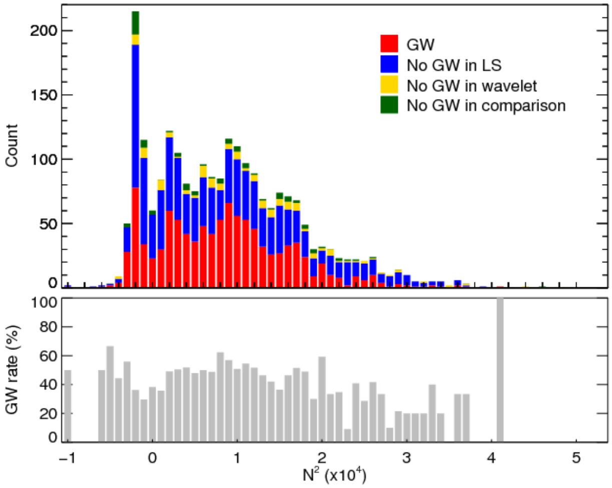

Figure R2. The histograms of GWs occurrence with squares of buoyancy frequency (upper panel). GWs occurrence rate versus buoyancy frequency (bottom panel).

not only with taking into account the magnitudes of wind velocity and wind shear, as it is presented in Fig. 6, but also with consideration of the temperature stratification.

Response: We revised the manuscript to make the goal of this study more clearly. The temperature profile measured with the radiosonde at 19:15 on 4th September in the revised Fig. 5. We had considered the temperature stratification N_2 before submit the manuscript. The result shows that there is not any significant relation between the frequency of wave events and temperature stratification as shown in Fig. R2.

However, the method of GW identification is simple and rough, not serious. As replied in major comment 8 to **Anonymous Referee #1**, we deleted the related text of GW identification and frequency of wave events in the revised manuscript due to following reason:

"During the revision, we reconsidered this part of GW identification. We present this part to demonstrate the relation between GW occurrences and background wind. However, on the one hand, this relation has been studied in several previous studies (Mahrt, 2014) and can be also analyzed in Sect. 4.2. On the other hand, the method if GW identification described in Appendix B is simple and rough, not serious as discussed in Appendix B. Therefore, we decided to delete these text and figure related to GW identification during the whole field campaign in the revised manuscript. The same to the Appendix B. This deletion will not affect the analysis and result of this work. At the same time, this deletion will also help us concentrate on the analysis of the unique long-lived ducted GW."

2) The representativeness of the estimates of the mean wind velocity. As mentioned in line 6 on p.4, measurement duration of radial velocity in one direction is 10 s during this experiment. For used in the experiment scanning geometry such duration of measurements is insufficient in order to obtain statistically justified estimates of the mean wind velocity components. Actually, it is well known that integral spatial scale of wind turbulence is proportional to the height under ground in the lower atmosphere and can reach a few hundreds of meters at the heights 600-2000 m. To obtain statistically justified estimate of the mean velocity, the velocity fluctuations caused by the turbulent inhomogeneities of all the scales up to hundreds of meters must be averaged. Even for observed in the experiment maximal

velocity 10 m/s in order to average velocity fluctuations caused by the turbulent inhomogeneities of velocity field of such spatial scales it requires few hundreds seconds, at least.

Response: We totally agree that "To obtain statistically justified estimate of the mean velocity, the velocity fluctuations caused by the turbulent inhomogeneities of all the scales up to hundreds of meters must be averaged." We have checked the raw radial wind in both north beam and west beam. The ducted wave motions are still significant. In addition, turbulence activity is relatively weak in the nocturnal residual layer. As shown in Fig. 2, wave motions are significant without average, though smoothed perturbation will be better in Fig. 7f. Hence, the turbulence inhomogeneities and average will not affect the result of this work. Though the amplitude of zonal/meridional wave motions may be affected due to the turbulence and wave motions.

3) What is the reason of variations of wave period in Figs 3, 4? Model calculations in Fig. 8 do not reproduce wave period variations. It may be useful to compare the experimental and calculation results in more detail by combining the experimental and calculated data in one plot. It is difficult to compare and understand the results in Figs. 8b, 8c.

Response: The variation of the wave period may be caused by turbulence and the change of background winds. The reason why model calculations do not reproduce wave period variation may be due to stable boundary condition in the model, while lidar observed wind may be affected by many reasons, such as terrain, weather system and so on. Thanks for the suggestion of the comparation. We think that a time-height cross section of vertical wind perturbation would be better with more information. Therefore, we added a panel of comparation of vertical wind perturbation at 1.0 altitude from both observation and simulation results in revised Fig. 8.

Changes: Fig. 8.

4) The code used for numerical modeling must be described in more detail. As it can be proposed, some version of the program CFD Fluent was used in the modeling. Accordingly to Eqs. (2), (3), it is required to set a lot of input turbulent parameters in order to perform the modeling using that code. None of these input parameters is determined experimentally. At least, there is no information about that in the

manuscript. If so, there is no any base for quantitative comparison of the experimental and computational results and conclusions about the mechanism of wave generation.

Response: The description of numerical simulations is reorganized with more details in Sect. 4.1. The input turbulent parameters recommended by OpenFOAM are applied (https://www.openfoam.com/documentation/guides/latest/api/classFoam_1_1RASModels_1_1RNGkEpsilon.htm). The default model coefficients of RNGkEpsilon are: $G_{1\epsilon} = 1.42$; $G_{2\epsilon} = 1.42$; $G_{3\epsilon} = -0.33$; $\alpha_k = 1$; $\alpha_\varepsilon = 1.22$.

Changes: Page 9, line 26 to page 10, line 18. "In this paper, the input turbulent parameters recommended by OpenFOAM are applied. The default model coefficients of RNG k-ε are: $G_{1\epsilon} = 1.42$; $G_{2\epsilon} = 1.42$; $G_{3\epsilon} = -0.33$; $\alpha_k = 1$; $\alpha_\varepsilon = 1.22$.

To simplify the numerical simulation processes, a two-dimensional (2D) rectangle computational domain is applied in this study. with 70 km in horizontal and 5 km in vertical from sea level. The upper interface extended to 5 km is set as symmetric condition to prevent the influence of upper interface on the region concerned that below 2 km. On this condition, zero gradient is set for all vertical physical variables, and the vertical velocity is set as zero. The vertical height of the first layer of grid cells is 5 m. The spatial resolution is approximately 20 m in both horizontal and vertical. The total number of computational grid cells is 875,000. The velocity-inlet is westerly and constant in the west boundary of the computational domain. The easterly interface is set as pressure-outlet boundary to improve reversed flow. The topography is set as no-slip wall condition. A rough-wall function is adopted, of which the formula is as follows (Ren et al., 2018):

$$\frac{u}{u^*} = \frac{1}{K} In(\frac{Ez_c}{Ck_s}) \tag{4}$$

where E=9.793 is the wall constant, C = 0.327 is a roughness constant, K≈0.4 is the von Karman constant, k_s is the roughness height, z_c is the distance to the cell center of the first wall adjacent cell, u is the velocity in the cell center, u^* is the friction velocity. The simulation is run with a time step of 0.5 s.

The CFD cases conducted in this study are used to reveal the influence of topography and wind shear on the generation of the persistent GWs. The thermal field is assumed to be uniform in a horizontal plane. Temperature profile from radiosonde on 5 September is applied in this model. In this work, buoyant flows are developed with low velocity and small temperature variations. As a result, the Boussinesq model is used in this work, which considers only the effect of buoyancy in gravity terms. The Boussinesq approximation can be used instead of a constant density. This model treats density as a constant value ρ_{ref} in all solved equations, except for the gravity and buoyancy term in the momentum equation. The density ρ is approximated as:

$$\rho = \rho_{ref} - \rho_{ref}\beta\left(T - T_{ref}\right) \qquad (5)$$

where β is the thermal expansivity, T_{ref} is a reference temperature."

Minor comments:

1) Temperature profile curves in Fig.5 should be identified.

Response: The temperature profile from radiosonde can be easily identified. We know that a shift of each temperature profile from ERA5 would be better. Nevertheless, the vertical structure of the temperature profiles can be still identified without a shift. An inversion layer is obvious under 0.5 km altitude.

2) Parameter N in line 14, p.7 should be expressed by formula.

Response: Added.

3) Resolution of wind and temperature experimental data in height should be indicated.

Response: Added.

4) Magnitudes of âˇDOA, and ãDOB in Fig.8 and Table 2 must be indicated.

Response: It may be assumed that âˇDOA (âˇDOB) is h_{A} (h_{B}).

Changes: Page 10, line 23. "The maximum elevation of A and B are approximately 250 m and 600 m, respectively."

References:

El Kasmi, A., and Masson, C.: Turbulence modeling of atmospheric boundary layer flow over complex terrain: a comparison of models at wind tunnel and full scale, Wind Energy, 13, 689-704, 10.1002/we.390, 2010.

Franke, J., Hirsch, C., Jensen, G., Krüs, H. W., Miles, S. D., Schatzmann, M., Westbury, P. S., Wisse, J. A., and Wright, N.: Recommendations on the use of CFD in wind engineering, Proceedings of the International Conference on Urban Wind Engineering and Building Aerodynamics, 2004.

Kim, H. G., Patel, V. C., and Lee, C. M.: Numerical simulation of wind flow over hilly terrain, Journal of Wind Engineering and Industrial Aerodynamics, 87, 45-60, 10.1016/s0167-6105(00)00014-3, 2000.

Luketa-Hanlin, A., Koopman, R. P., and Ermak, D. L.: On the application of computational fluid dynamics codes for liquefied natural gas dispersion, Journal of hazardous materials, 140, 504-517, 10.1016/j.jhazmat.2006.10.023, 2007.

Mahrt, L.: Stably Stratified Atmospheric Boundary Layers, Annual Review of Fluid Mechanics, 46, 23-45, 10.1146/annurev-fluid-010313-141354, 2014.

Miller, C. A., and Davenport, A. G.: Guidelines for the calculation of wind speed-ups in complex terrain, Journal of Wind Engineering and Industrial Aerodynamics, 74-76, 189-197, 10.1016/s0167-6105(98)00016-6, 1998.

Orszag, S. A.: Renormalisation group modelling and turbulence simulations, Near-wall turbulent flows, Tempe, Arizona, 1993.

Ren, H., Laima, S., Chen, W.-L., Zhang, B., Guo, A., and Li, H.: Numerical simulation and prediction of spatial wind field under complex terrain, Journal of Wind Engineering and Industrial Aerodynamics, 180, 49-65, 2018.

Toparlar, Y., Blocken, B., Maiheu, B., and van Heijst, G. J. F.: A review on the CFD analysis of urban microclimate, Renewable and Sustainable Energy Reviews, 80, 1613-1640, 10.1016/j.rser.2017.05.248, 2017.

Tran, V., Ng, E. Y. K., and Skote, M.: CFD simulation of dense gas dispersion in neutral atmospheric boundary layer with OpenFOAM, Meteorology and Atmospheric Physics, 10.1007/s00703-019-00689-2, 2019.

Walmsley, J. L., Taylor, P. A., and Salmon, J. R.: Simple guidelines for estimating windspeed variations due to small-scale topographic features–an update, Climatological bulletin, 23, 3-14, 1984.

Yakhot, V., Orszag, S., Thangam, S., Gatski, T., and Speziale, C.: Development of turbulence models for shear flows by a double expansion technique, Physics of Fluids A: Fluid Dynamics, 4, 1510-1520, 1992.

Yan, B. W., Li, Q. S., He, Y. C., and Chan, P. W.: RANS simulation of neutral atmospheric boundary layer flows over complex terrain by proper imposition of boundary conditions and modification on the k-ε model, Environmental Fluid Mechanics, 16, 1-23, 10.1007/s10652-015-9408-1, 2015.

Long-~~live~~lived high frequency gravity waves in the atmospheric boundary layer: observations and simulations

Mingjiao Jia[1,*], Jinlong Yuan[1,2,*], Chong Wang[1,2], Haiyun Xia[1,2], Yunbin Wu[2], Lijie Zhao[2], Tianwen Wei[2], Jianfei Wu[2], Lu Wang[2], Sheng-Yang Gu[3], Liqun Liu[4], Dachun Lu[5], Rulong Chen[5], Xianghui Xue[2], Xiankang Dou[3]

[1]Glory China Institute of Lidar Technology, Shanghai, 201315, China
[2]CAS Center for Excellence in Comparative Planetology, University of Science and Technology of China, Hefei, 230026, China
[3]School of Electronic Information, Wuhan University, Wuhan, 430072, China
[4]Anqing Meteorological Bureau, China Meteorological Administration, Anqing, 246001, China
[5]Technical Support Center for Atmosphere Observation, Anhui Meteorological Administration, Hefei, 230031, China
[*]These authors contributed equally to this work.

Correspondence to: Haiyun Xia (hsia@ustc.edu.cn)

Abstract. A long-~~live~~lived gravity wave (GW) in atmospheric boundary layer (ABL) during a field experiment in Anqing, China (116 °58′ E, 30 °37′ N) is analysed. Persistent GWs over 10 hours with periods ranging from 10 to 30 min in the ABL within 2 km height are detected by a coherent Doppler lidar from 4 to 5 in September 2018. The amplitudes of the vertical wind due to these GWs are about 0.15~0.2 m s^{-1}. The lifetime of the GWs is more than 20 wave cycles. There is no apparent phase progression with altitude. The vertical and zonal perturbations of the GWs are ~~apparent quadrature~~90 °out of phase with vertical perturbations generally leading ahead of zonal ones. Based on experiments and simplified 2-Dimensional Computational Fluid Dynamics (CFD) numerical simulations, a reasonable generation mechanism of this persistent wave is proposed. A westerly low-level jet of ~5 m s^{-1} exists at the altitude of 1~2 km in the ABL. The wind shear around the low-level jet lead to the wave generation in the condition of light horizontal wind. Furthermore, a combination of thermal and Doppler ducts occurs in the ABL. Thus, the ducted wave motions are trapped in the ABL with long lifetime.

1 Introduction

The atmospheric boundary layer (ABL) is the most important atmospheric environment affecting the human life. Gravity waves (GWs) and corresponding physical processes have important impacts on synoptic systems, atmospheric models, aircraft take-off and landings in the ABL (Clark et al., 2000; Fritts and Alexander, 2003; Holton and Alexander, 2000; Sun et al., 2015b). GWs are ubiquitous in the atmosphere and usually generated from topography, convection, wind shear, jet streams, frontal systems and other sources in the troposphere (Banakh and Smalikho, 2016; Blumen et al., 1990; Chouza et al., 2016; Fritts and Alexander, 2003; Plougonven and Zhang, 2014; Pramitha et al., 2015; Toms et al., 2017; Wu et al., 2018)~~. As propagating upward, GWs will become unstable or break when a critical layer is encountered. On the one hand, these breaking GWs would cause clear air turbulence, which is hazardous to aircraft as it is neither visible to pilots nor detectable by standard~~

~~on-board radars . On the other hand, these processes will lead~~. In general, most of these GWs will propagate upward into the upper atmosphere, e.g. upper troposphere, stratosphere, mesosphere and even thermosphere. Leading to transportation of energy and momentum from lower atmosphere to upper atmosphere, and thus affect the coupling between lower atmosphere and upper atmosphere, as well as dynamic and thermal structure of the global atmosphere (Fritts and Alexander, 2003; Holton and Alexander, 2000). However, trapped GWs, e.g. trapped lee waves and ducted motions with high frequency and coherent variability, could only propagate horizontally. In the lower atmosphere, these horizontally propagating GWs may be linked to low level turbulence (e.g. rotors), the initiation of convection and low level wave drag (Birch et al., 2013; Grubišić et al., 2008; Lac et al., 2002; Lapworth and Osborne, 2016; Marsham and Parker, 2006; Tsiringakis et al., 2017)~~. Therefore, GW plays a key role in aviation safety, weather forecast and climate models~~. Therefore, such trapped GWs play a key role in weather forecast, climate models and aviation safety.

In the ABL, except lee waves, ducted GWs are mainly high frequency GWs with periods less than one hour ~~contribute most to transporting momentum into upper atmosphere~~in previous studies (Banakh and Smalikho, 2018; Banakh and Smalikho, 2016; Fritts et al., 2003; Viana et al., 2009). However, these GWs and their sources are difficult to be resolved in global general circulation models due to smaller spatial and temporal scales. Only mesoscale and larger scale GWs can be resolved in global atmospheric models (Preusse et al., 2014; Wu et al., 2018). GW parameterizations are always used in global models to increase their reliability and precision (Fritts and Alexander, 2003). Thus there is requirement to improve our understanding of high frequency ducted GWs and their sources.

However, wave motions in the ABL are usually difficult to be detected due to the contaminations from strong turbulence. Therefore, most wave motions are observed in the stably stratified ABL (Banakh and Smalikho, 2016; Fritts et al., 2003; Mahrt, 2014; Sun et al., 2015a; Sun et al., 2015b; Toms et al., 2017). These wave motions can be maintained more than a few periods if atmospheric wave ducting properties are present, while such monochromatic waves are infrequently observed (Mahrt, 2014; Toms et al., 2017). In addition, due to the capabilities of ground-based measurements, most of these previous studies are limited to the surface layer within tens or hundreds of meters near the ground, not the whole ABL.

Numerous instruments have been utilized to detect wave motions in the ABL. Fixed point measurements on a tower or surface (Einaudi and Finnigan, 1981; Finnigan and Einaudi, 1981; Poulos et al., 2002; Sun et al., 2015a; Sun et al., 2004), in-situ measurements on mobile platform such as balloon (Corby, 1957), aircraft (Fritts et al., 2003; Kuettner et al., 2007), remote sensing measurements such as sodar (Beran et al., 1973; Hooke and Jones, 1986; Lyulyukin et al., 2015), radar (Cohn et al., 1997; Cohn et al., 2001) and lidar (Chouza et al., 2016; Mayor, 2017; Neiman et al., 1988; Newsom and Banta, 2003; Poulos et al., 2002; Witschas et al., 2017) are widely used in recent decades. All these techniques are sensitive to only a certain portion of the wave spectra and wave characteristics, given a limited spatial and temporal range. Among these instruments, lidar can make measurements alone with sufficient long detection range, multi scanning mode, high temporal/spatial resolution. Recently, a micro-pulse coherent Doppler lidar (CDL) is developed to measure wind field with temporal resolution of 2 s and spatial resolution of 60 m in ABL (Wang et al., 2017). Wave motions such as high frequency GWs can be revealed from the vertical wind measured by this lidar in the whole ABL.

Numerical simulations are also used to study GWs. Mesoscale and large scale GWs can be resolved in high spatial and temporal resolution models such as Whole Atmosphere Community Climate Model (WACCM) and Weather Research and Forecasting (WRF) (Wu et al., 2018). For high frequency GWs with smaller scales, high resolution Computational Fluid Dynamics (CFD) simulations have been used in recent years (Chouza et al., 2016; Watt et al., 2015). CFD simulation is able to resolve the flow field at different spatial scales, ranging from mesoscale of ~200 km to indoor environment of ~10 m (Berg et al., 2017; Fernando et al., 2018; Mann et al., 2017; Remmler et al., 2015; Ren et al., 2018; Toparlar et al., 2015; Toparlar et al., 2017; Vasiljević et al., 2017; Watt et al., 2015). With the help of CFD simulation, the generation mechanism and characteristics of GWs can be resolved, as well as the subsequent evolutions of GWs.

In this paper, we report long~~-live~~lived high frequency GWs in the whole ABL detected by the CDL. The characteristics and the generation mechanism are analysed using experiments and CFD simulations. Section 2 describes the field experiments and instruments used in this study. Section 3 presents the observational results~~ and corresponding analysis of the GWs.~~. The CFD model and simulation results are described and discussed in Sect. 4. Section 5 gives a discussion of the generation mechanism of the persistent GWs. Finally, the conclusion is drawn in Sect. 6. If not specified, local time is used in this paper.

2 Experiments and instruments

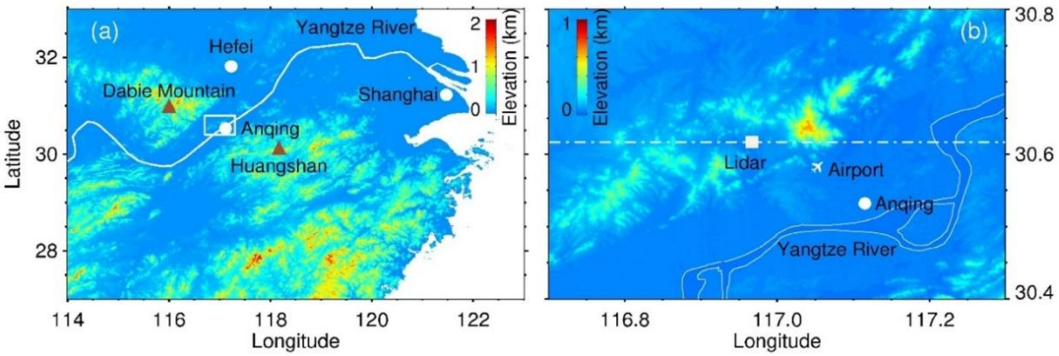

Figure 3. (a) Terrain elevation map. (b) Zoom over Anqing station in the white hollow rectangle in (a). The computational domain is roughly along the white dash dotted line in latter numerical simulations.

A field experiment is conducted to study the generation mechanism of GWs by the CDL in National Meteorological Observing Station of Anqing (116 °58′ E, 30 °37′ N) from 16 August to 5 September 2018. Anqing is located near Yangtze River and between Huangshan (118 °10′ E, 30 °08′ N) in the southeast and Dabie Mountain (115 °~117 °E, 30 °~32 °N) in the southwest as shown in Fig. 1a. The station is surrounded by hills with relative elevation of 200~600 m as shown in Fig. 1b. An airport is located in the southeast of the station.

2.1 Coherent Doppler wind lidar

A compact micro-pulse CDL working at eye-safe wavelength of 1.5 μm is used in this study. The pulse duration and pulse energy of the laser are 300 ns and 110 μJ, respectively. A double D-shaped telescope is employed. The absolute overlap distance and blind distance are ~1 km and 60 m, respectively. This lidar has full hemispheric scanning capability with the rotatable transmitting and receiving system. Benefiting from the coherent detection, this lidar can perform all-day measurement of radial wind speed based on the Doppler effect. Compared with traditional lidars, this CDL is small in size and robust in stability due to the all-fiber configuration. More details of this lidar are described in Wang et al. (2017). The key parameters of the CDL are listed in Table 1.

Table 1. Key Parameters of the CDL

Parameter	Value
Wavelength	1548 nm
Pulse Duration	300 ns
Pulse Energy	110 μJ
Repetition frequency	10 kHz
Diameter of telescope	80 mm
Spatial resolution	60 m
Temporal resolution	2 s
Maximum range	15 km
Azimuth scanning range	0 - 360 °
Zenith scanning range	0 - 90 °

Wind ~~filed~~field is composited by pointing the rotatable scanner at three directions during the experiment. Firstly, the laser beam is pointed at two orthogonal azimuths sequentially, north and west with a zenith angle of 30 °. Then, the laser beam is pointed vertically upward. In each direction, the measurement duration is set to 10 s during this experiment. The full period of the measurement cycle is 41 s. The observational results, such as vertical and horizontal wind components, and carrier to noise ratio (CNR) in the vertical beam, are shown in Appendix A. The blank areas without measurements are owing to the rainy summer. For example, the No. 18 Typhoon Rumbia passed by around 17 August 2018. To guarantee the precision of the wind measurements, the data with CNR less than -35 dB is abandoned (Wang et al., 2017; Wang et al., 2019).

2.2 Radiosonde

National Meteorological Observing Station of Anqing is one of the 120 operational radiosonde stations in China (excluding Hong Kong and Taiwan) (Li, 2006). China Meteorological Administration has deployed an L-band (1675 MHz) sounding system in this station. Air temperature, pressure, relative humidity and wind from the ground to middle stratosphere can be measured twice a day at 07:15 and 19:15 by this sounding system, which combines a GTS1 digital radiosonde with a secondary wind-finding radar. Previous studies confirmed the accuracy measured by this type of radiosonde (Bian et al., 2010).

2.3 ERA5 reanalysis data

ERA5 is the fifth generation of ECMWF (European Centre for Medium-Range Weather Forecasts) atmospheric reanalysis of the global climate. ERA5 reanalysis assimilates a variety of observations and models in 4-~~dimensional~~dimensions. The data has 137 levels from the surface up to 80 km altitude and horizontal resolution of 0.3 °for both longitude and latitude (Hersbach and Dee, 2016). The hourly temperature data from high resolution realisation sub-daily deterministic forecasts of ERA5 is used to calculate buoyancy frequency near the station in latter analysis in this study.

3 Observations and analysis

3.1 The long-~~live~~lived GWs

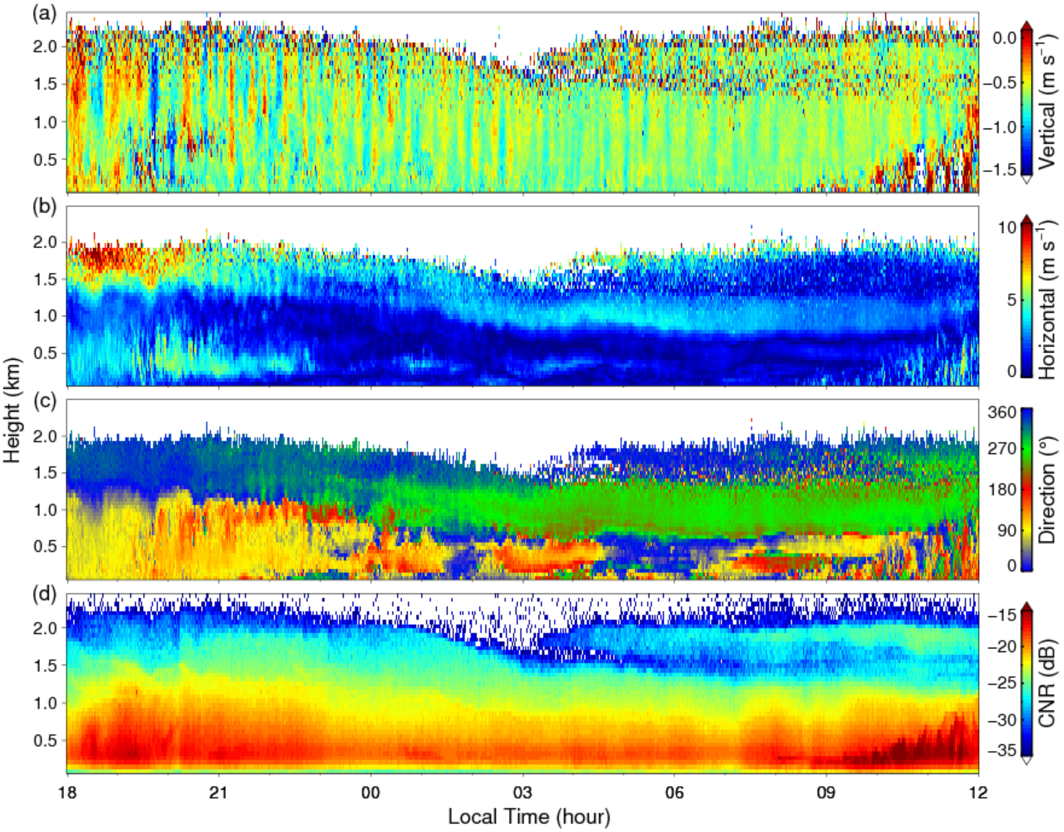

Figure 2. Height-time cross sections of the (a) vertical wind, (b) horizontal wind speed, (c) horizontal wind direction and (d) CNR in vertical obtained by the CDL from 4 to 5 September 2018. The direction is defined as the angle clockwise from the north.

Figure 2a shows the persistent wave motions in the vertical wind longer than 10 hours in the ABL between 4 and 5 September 2018. These waves exist more than 20 periods and then dissipated during the evolution of convective ABL in the morning on 5 September 2018. The corresponding horizontal wind speed and wind direction are shown in Fig. 2b and 2c. Two weak low-level jets are observed at heights of about 0.5 and 1.5 km. The lower easterly jet stream lasts only a few hours with speed of about 5 m s^{-1}, while the higher jet stream exists during the whole lifetime of the wave motions. The speed of the higher jet stream is about 10 m s^{-1} and then decreases to about 3~5 m s^{-1} after 21:00. The corresponding direction of this northerly jet stream is also changed to westerly. The CNR from the vertical beam is shown in Fig. 2d, which varies slowly with time and nearly stratified in altitude. Thus the ABL ~~is~~seems to be stably stratified as the CNR may represents the aerosol concentration in some cases.

The periods of these wave motions are typically about 10~30 minutes. The temporal profiles of average vertical wind between 600 m and 1000 m is plotted in Fig. 3a. Oscillations of vertical wind can be seen clearly. The amplitudes of these wave motions are about 0.2 m s^{-1} before 03:00 and then decreases to about 0.15 m s^{-1} while the periods extended after 04:00. The wavelet power spectrum of the vertical wind in Fig. 3a is shown in Fig. 3b by using the Morlet mother wavelet. There are obvious waves with periods of 15~25 min before 03:00 and waves with periods of 20~30 min after ~04:30. Relatively weak waves with periods of about 10 min are also observed between 03:00 and 05:00. These wave motions could be regarded as quasi monochromatic waves as the periods varies within the range of 15~30 min. The change of periods may be in relation to the changes of the background ABL, such as the height of upper jet stream.

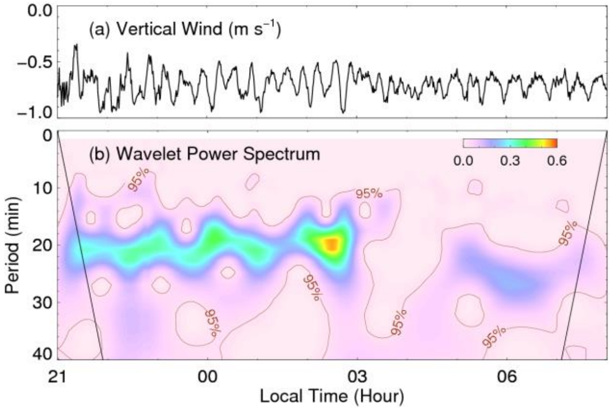

Figure 3. (a) Mean vertical wind between 600 m and 1000 m. (b) Corresponding wavelet power spectrum of the vertical wind in (a). The brown contours indicate significance level of 95%. The black solid lines represent the ~~Corn~~Cone-of-Influence.

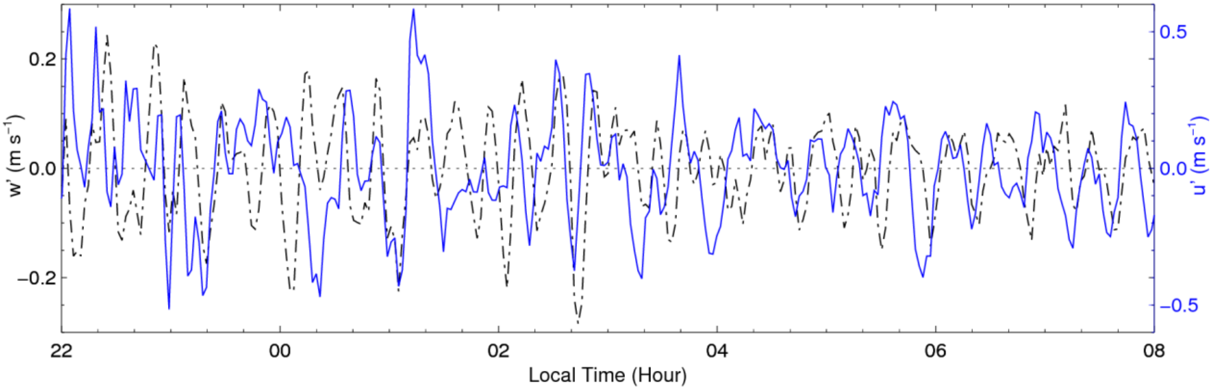

Figure 4. Perturbations of vertical wind $\mathbf{w}'$ (black dash dotted, left axis) and zonal wind $\mathbf{u}'$ (blue solid, right axis) obtained between 600 m and 1000 m altitude from 22:00 on 4 September to 08:00 on 5 September 2018.

Zonal wind can be derived from the horizontal wind speed and direction. The height averaged perturbations of vertical wind $\mathbf{w}'$ and zonal wind u' between 600 m and 1000 m altitude are shown in Fig. 4. First, the raw vertical/zonal wind are averaged with altitude between 600 m and 1000 m. Second, the temporal profile of averaged vertical/zonal wind is smoothed by a 1-hour window as the background. Thirdly, the background is subtracted to remove the trend. Finally, the perturbation is smoothed by averaging the adjacent three points to reduce high frequency noises. It is obvious that the wave motions also exist in the horizontal wind. The periods of the zonal perturbations are similar to that of vertical perturbations. Specifically, vertical and zonal perturbations are ~~apparent quadrature~~90 ° out of phase with vertical perturbations ~~$\mathbf{w}'$~~w' generally leading zonal perturbations u', especially after 02:00. Note that the wave motions exhibit highly coherent vertical motions with no apparent phase progression with altitude as shown in Fig. 2a. These characteristics of these wave motions indicate ducting wave structures within the ABL (Fritts et al., 2003).

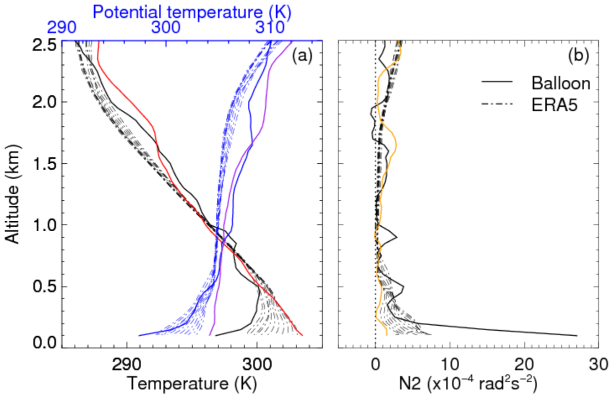

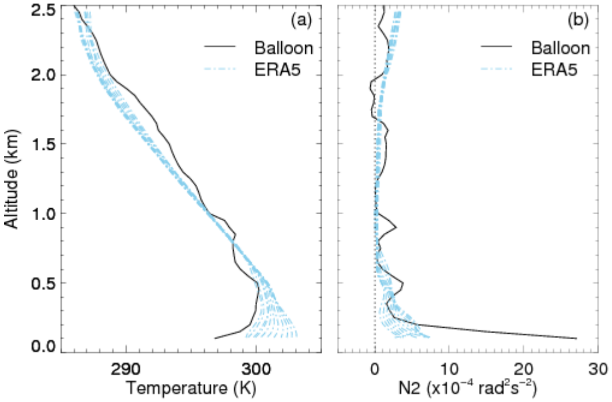

Figure 5. (a) Temperature (black solid line) and potential temperature profiles from radiosonde (~~black~~and blue solid~~)~~ line) at 07:15 on 5 September and ERA5 (~~skyblue~~ dot dashed~~) during the wave motions.~~ lines)betwwen 22:00 on 4 September and 08:00 on 5 September. (b) Corresponding buoyancy frequencies. Profiles of Temperature ~~**profile**~~ (red solid line), potential temperature (purple solid line) and buoyancy frequency (orange solid line) from radiosonde at 19:15 on 4 September are also plotted.

Temperature profiles measured by the radiosonde lifted on a balloon ~~at about 07:15 on 5 September 2018~~ and hourly temperature profiles from ERA5 ~~between 22:00 on 4 September and 08:00 on 5 September~~during the wav emotions are shown in Fig. 5a. An inversion layer is observed under altitude of ~500 m. The corresponding squares of buoyancy frequency ~~(N^2)~~ :

$$N^2 = \frac{g}{\theta}\frac{\partial\theta}{\partial z} \qquad (1)$$

are plotted in Fig. 5b~~.~~, where g is gravitational acceleration, θ is the potential temperature at altitude z. Maxima values of N^2 larger than 5×10^{-4} ~~$rad^2 s^{-2}$~~$\mathrm{rad}^2\mathrm{s}^{-2}$ appear in the inversion layer from both radiosonde and ERA5, indicating a strongly stratified stable boundary layer near ground. Between ~600 and ~2000 m altitude, the values of N^2 are so small that close to zero, even negative at 1800~2000 m from radiosonde. ~~There are no obvious wave motions above this region between 04:00~09:00 in the vertical wind as shown in Fig. 2a, though with large enough CNR in Fig 2d. These results also~~These results hint a thermal ducting between the ground and about ~2000 m, in which the wave motions are trapped, especially under the inversion. This is why such wave motions have a long lifetime longer than 20 periods. The buoyancy periods from Fig. 5b are typically 2~10 min. Since the background wind speeds are relatively small, less than ~10 m s^{-1}, we neglect Doppler effects here. These wave motions should be GWs instead of internal acoustic waves. Therefore, these waves are suggested to be ducted gravity waves trapped in the ABL.

3.2 Background wind

There are complex relationships between GWs and background wind conditions. Submeso wavelike motions, that any nonturbulent motions on horizontal scales smaller than 2 km and with periods of tens of minutes, are primarily generated in very weak winds in nocturnal boundary layer (Mahrt, 2014). Noted that the wind speed~~ and wind shear~~ from 4 to 5 in September 2018 are weakest during the whole field experiment in Fig. A2. In order to understand the relationship between ~~GWs ~~this ducted GW and background wind, ~~dominant GW are identified using the method described in Appendix B in each ~~a temporal ~~-~~spatial window~~. Here we focused on high frequency GWs with periods~~ of ~~10~50 min during the whole experiment. Therefore, a window of 4~~1-hour length and 200-m height, and shifted in steps of 1 hour temporally and 100 m vertically is used. ~~For the background wind, ~~Mean horizontal wind speed and wind direction in ~~the central 1-hour of ~~each window during the whole field campaign in Anqing are easily obtained. ~~Wind shear *S* can be calculated from the vertical profiles of mean horizontal wind speed, in which *S* is defined as below:~~

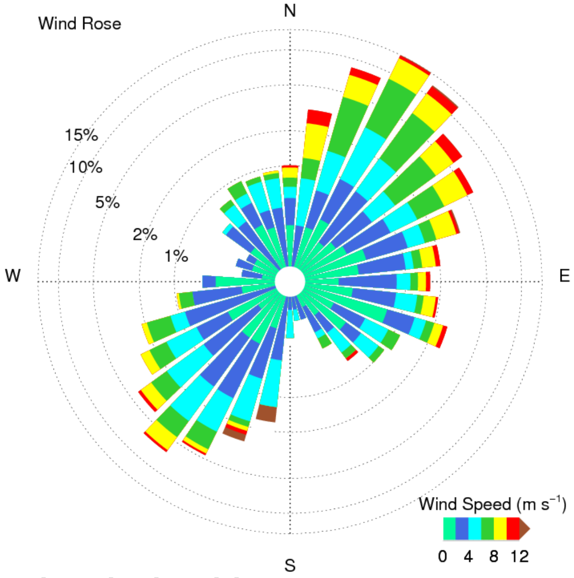

Figure 6. Wind rose of horizontal wind in all temporal spatial window during this experiment. It should be noted that the value of the radius is logarithmic.

~~$S = ((dU/dz)^2 + (dV/dz)^2)^{1/2}$ (1)~~

~~where *U* (*V*) is the zonal (meridional) wind speed and z is the height.~~

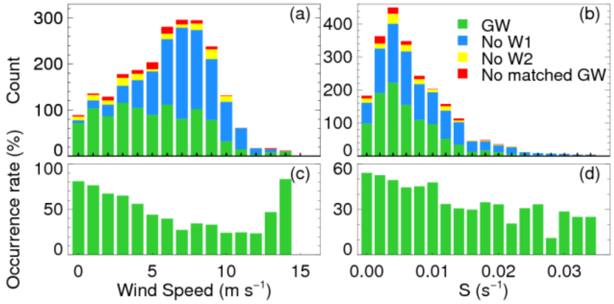

~~**Figure 6.** The histograms of GWs occurrence with (a) horizontal wind speed and (b) wind shear *S*. The green, blue, yellow and red bars represent the counts of windows with dominant GWs, without potential GWs W1, without W2, without W1 and W2 matched, respectively. W1 and W2 are defined in Appendix B and Fig. B1. GWs occurrence rate versus (c) horizontal wind speed and (d) wind shear *S*.~~

~~The histograms of GW occurrence with horizontal wind speed and wind shear in all temporal spatial windows are shown in Fig. 6a and 6b, respectively. The corresponding relationships between GW occurrence rate and horizontal wind speed and wind shear are shown in Fig. 6c and 6d, respectively. It is significant that weaker horizontal wind and weaker wind shear are beneficial to GWs occurrence in ABL from these results. Thus it could be inferred that weak wind and weak wind shear are favorable to the existence of such high frequency wave motions.~~

The wind rose of the horizontal wind during the field experiment is shown in Fig. ~~7a~~6. It is apparent that northeasterly wind and southwesterly wind are prevailing around the station in the ABL~~.~~ during the whole field campaign. The infrequently observed ducted GWs in Fig. 2 occur accompanying infrequently westerly weak wind. It is interesting to note that the long-narrow plain area along Yangtze River around Anqing between Huangshan and Dabie Mountain is also along the direction of northeast-southwest as shown in Fig. 1a. The typical elevations of Huangshan and Dabie Mountain are about 1~2 km. Strong wind along northwest-southeast direction may be blocked in the ABL, thus leading to the weak wind along northwest-southeast direction after the wind flowing over Huangshan or Dabie Mountain and the prevailing wind along northeast-southwest direction. ~~The azimuthal distribution of GW occurrence rate is presented in Fig. 7b. GW occurrence rates are relatively higher along the northwest-southeast direction than that along the northeast-southwest direction. Interestingly, it seems that the azimuthal distribution of GW occurrence rate is quadrature with the corresponding wind rose. Considering the azimuthal distribution of GW occurrence rate only under weak wind conditions (with horizontal speed less than 4 m s^{-1}), the GW occurrence rates are still relatively higher along the northwest-southeast direction, which is not shown here. The effect of weak wind on GW occurrence can be excluded here. Hence~~As GWs are favour to generate in weak wind conditions. we can imagine that Dabie Mountain and Huangshan may have an impact on GWs in Anqing. However, surrounding hills around the station as shown in Fig. 1b may also affect the generation and existence of GWs. The effect of surrounding hills will be studied by numerical simulations in next section.

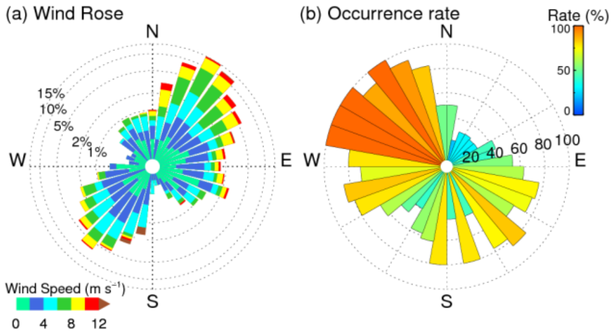

~~Figure 7. (a) Wind rose of horizontal wind in all temporal spatial window during this experiment. It should be noted that the value of the radius is logarithmic. (b) The azimuthal distribution of GW occurrence rates for every 10 °azimuth angle.~~

4 CFD simulations

Wavelike motions are common in the stably stratified ABL that maybe generated by topography or jet stream (Mahrt, 2014). There is a complex topography around the station as shown in Fig. 1b and a low-level jet in the ABL as shown in Fig. 2. Both of them may be responsible for the generation of the persistent GWs. In order to identify the potential source of the ducted GWs, a numerical simulation based on CFD is performed to simulate the fluid flow field. ~~Numerical simulations with CFD have better accuracies than mesoscale model for atmospheric flow dynamics in the ABL .~~ The impact of different boundary conditions, e.g., wind profile and topography, on atmospheric dynamics can be effectively evaluated by changing the boundary conditions. In addition, the numerical simulations can provide the full information of the GWs, which cannot be detected by lidar in this experiment, such as horizontal wavelength, horizontal phase speed and so on. Therefore, CFD simulations are helpful to investigate GWs in the ABL.

4.1 Model description

Reynolds-averaged Navier-Stokes Simulation (RANS) has been widely used to investigate wind field over the past few decades (Toparlar et al., 2017). Compared with Large Eddy Simulation (LES), RANS has advantages of low computational cost and the sufficient accuracy. In this study, a two-equation RANS model based on renormalisation group (RNG) methods is used to simulate wind ~~filed~~field. The RNG k-ε model was developed to renormalize the Navier-Stokes equations which are account for the effects of smaller scale motions (Yakhot et al., 1992). The RNG k-ε model is a quite mature model which is widely verified in simulation of wind flow over complex terrain in recent years (El Kasmi and Masson, 2010; Yan et al., 2015)~~.~~. The RNG k-ε turbulence model used in this work is based on OpenFOAM. OpenFOAM is the leading free, open source software for CFD simulations. The model transport equations are obtained as follows:

$$\frac{\partial}{\partial t}(\rho k)+\frac{\partial}{\partial x_i}(\rho k u_i)=\frac{\partial}{\partial x_j}\left(\alpha_k \mu_{eff}\frac{\partial k}{\partial x_j}\right)+G_k+G_b-\rho\varepsilon-Y_M+S_k \qquad (2)$$

$$\frac{\partial}{\partial t}(\rho\varepsilon)+\frac{\partial}{\partial x_i}(\rho\varepsilon u_i)=\frac{\partial}{\partial x_j}\left(\alpha_\varepsilon \mu_{eff}\frac{\partial \varepsilon}{\partial x_j}\right)+G_{1\epsilon}\frac{\epsilon}{k}(G_k+C_{3\varepsilon}G_b)-C_{2\epsilon}\rho\frac{\varepsilon^2}{k}-R_\varepsilon+S_\varepsilon \qquad (3)$$

where t and ρ are time and air density, k and ε are turbulence kinetic energy (TKE) and TKE dissipation rate, x_i and x_j are the displacement in dimension i and j, u_i is velocity in dimension i, α_k and α_ε are the inverse effective Prandtl numbers for k and ε, μ_{eff} is effective viscosity, G_k and G_b represent the generation of TKE due to the mean velocity gradients and buoyancy, Y_M represents the contribution of the fluctuating dilatation in compressible turbulence to the overall dissipation rate, S_k and S_ε are user-defined source terms, $G_{1\epsilon}$, $C_{2\epsilon}$ and $C_{3\varepsilon}$ are constants. In this paper, the input turbulent parameters recommended by OpenFOAM are applied. The default model coefficients of RNG k-ε are: $G_{1\epsilon} = 1.42$; $G_{2\epsilon} = 1.42$; $G_{3\epsilon} = -0.33$; $\alpha_k = 1$; $\alpha_\varepsilon = 1.22$.

To simplify the numerical simulation processes, a two-dimensional (2D) rectangle computational domain is applied in this study. with 70 km in horizontal and 5 km in vertical from sea level. The upper interface extended to 5 km is set as symmetric condition to prevent the influence of upper interface on the region concerned that below 2 km. On this condition, zero gradient is set for all vertical physical variables, and the vertical velocity is set as zero. The vertical height of the first layer of grid cells is 5 m. The spatial resolution is approximately 20 m in both horizontal and vertical. The total number of computational grid cells is 875,000. The velocity-inlet is westerly and constant in the west boundary of the computational domain. The easterly interface is set as pressure-outlet boundary to improve reversed flow. The topography is set as no-slip wall condition. A rough-wall function is adopted, of which the formula is as follows (Ren et al., 2018)~~The simulation is run with a time step of 0.5 s.~~:

~~4.2 Numerical simulations~~

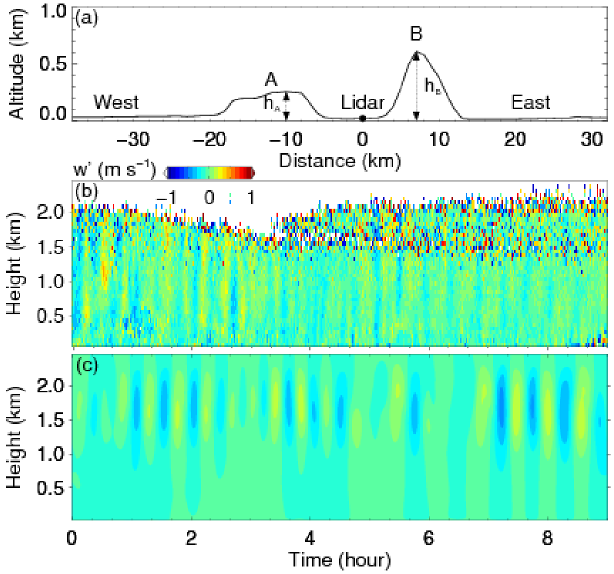

~~Figure 8. (~~$\frac{u}{u^*} = \frac{1}{K} In(\frac{Ez_c}{Ck_s})$ (4)

where E=9.793 is the wall constant, C = 0.327 is a~~)~~ roughness constant, K≈0.4 is the von Karman constant, k_s is the roughness height, z_c is the distance to the cell center of the first wall adjacent cell, u is the velocity in the cell center, u^* is the friction velocity. The simulation is run with a time step of 0.5 s.

The CFD cases conducted in this study are used to reveal the influence of topography ~~used in CFD simulations. A/B represents west/east hill.~~ ~~$\boldsymbol{h_\mathrm{A}}$~~ and ~~$\boldsymbol{h_\mathrm{B}}$ represent the height of A and B. (b) The vertical~~ wind ~~perturbation~~shear on the generation of the persistent GWs. The thermal field is assumed to be uniform in a horizontal plane. Temperature profile from ~~lidar during 00:00~09:00 LT in~~ radiosonde on 5 September ~~2018. A mean~~is applied in this model. In this work, buoyant flows are developed with low velocity and small temperature variations. As a result, the Boussinesq model is used in this work, which considers only the effect of buoyancy in gravity terms. The Boussinesq approximation can be used instead of a constant density. This model treats density as a constant value ~~is subtracted. (c) The CFD simulated results of vertical wind.~~ ρ_{ref} in all solved equations, except for the gravity and buoyancy term in the momentum equation. The density ρ is approximated as:

$$\rho = \rho_{ref} - \rho_{ref}\beta\left(T - T_{ref}\right) \qquad (5)$$

where β is the thermal expansivity, T_{ref} is a reference temperature.

4.2 Numerical simulations

The initial smoothed topography is shown in Fig. ~~8a~~7a. The horizontal location of the domain is roughly along the zonal white dash dotted line in Fig. 1b. This is because the low-level jet and the background wind are mainly in the zonal (east-west) direction. The left (west) hill is defined as A with height of h_A, as well as B with height of h_B for right (east) hill in this study. The maximum elevation of A and B are approximately 250 m and 600 m, respectively. The lidar is located between A and B. The 1-hour mean zonal wind under 2 km from lidar and zonal wind above 2 km from ERA5 reanalysis data at 00:00 in 5 September 2018 are merged as the sustained import wind profile u_0 in the west boundary of the computational domain. The vertical profile of potential temperature and u_0 used in the CFD models are shown in Fig. 7b and 7c. The measured vertical wind perturbation w' subtracted by a mean value is shown in Fig. ~~8b~~7d. The vertical wind from CFD simulations is shown in Fig. ~~8c~~7e. The measured and simulated vertical perturbation at 1.0 km are compared in Fig. 7f. It is obvious that a similar wave motion with similar amplitude and period exists in the ABL. This result verifies the accuracy of the CFD numerical simulation results in this study. A small movie of the zonal wind and vertical wind in the whole computational domain can be downloaded from the Supplement. From this movie, the zonal wavelength can be estimated as ~3 km, and the corresponding zonal phase speed of ~2 m s^{-1}. In addition, Kelvin-Helmholtz billows exist in the low-level jet around the altitude of 2 km. These billows may be in relation to these GWs.

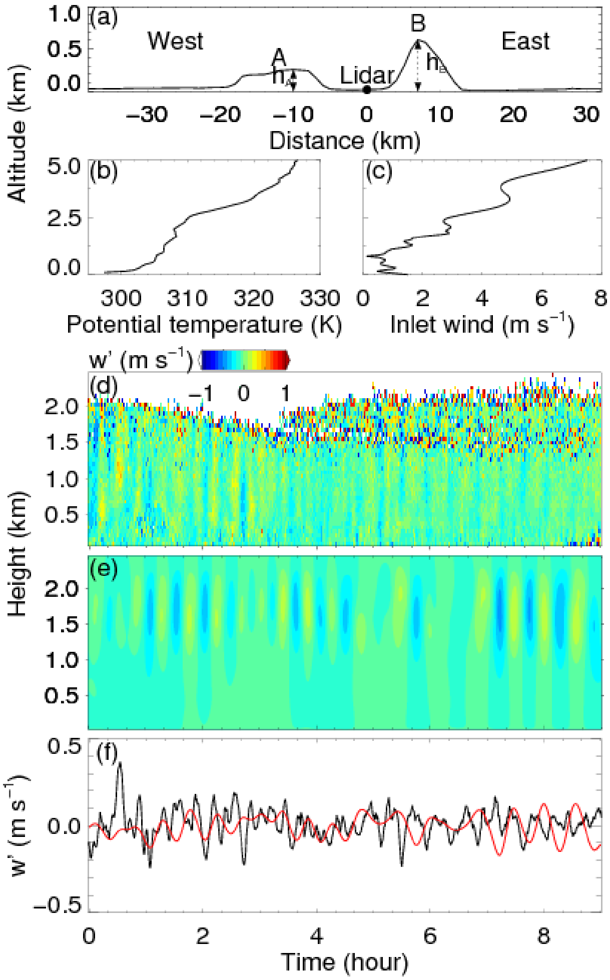

Figure 7. (a) The topography used in CFD simulations. A/B represents west/east hill. h_A and h_B represent the height of A and B. (b) The vertical profile of potential temperature used in the CFD model. (c) The vertical profile of the inlet wind in the CFD model. (d) The vertical wind perturbation from lidar during 00:00~09:00 LT in 5 September 2018. A mean value is subtracted. (e) The CFD simulated results of vertical wind. (f) Observed (black) and simualted (red) vertical pertubations at 1 km altitude. The observed pertubation is smoothed with five-point smoothing.

~~**Table 2.** The wind profile and topography for each case in CFD simulations.~~

Based on this result, wind profiles u_z with different wind shear and topography with different height of hills A and B are employed in the CFD numerical simulations. A detailed boundary conditions are listed in Table 2. The ~~merged zonal wind at 00:00 in 5 September 2018 used in Fig. 8 is defined as u_0. The~~ corresponding simulated results of zonal wind and vertical wind above the lidar for all cases are shown in Fig. ~~9~~8, respectively. It should be noted that the ~~flow solution is initiated as~~time of 0 represents a steady state in all cases except case 7 and 8. Here, the steady state means the state when the turbulence developed fully, i.e., when the wind-inlet passed by the ABL and varies regularly above lidar station. In case 7 and case 8, the ~~start~~ time of 0 is defined as when the simulations started running and the velocity-inlet flowed from the west boundary at the same time.

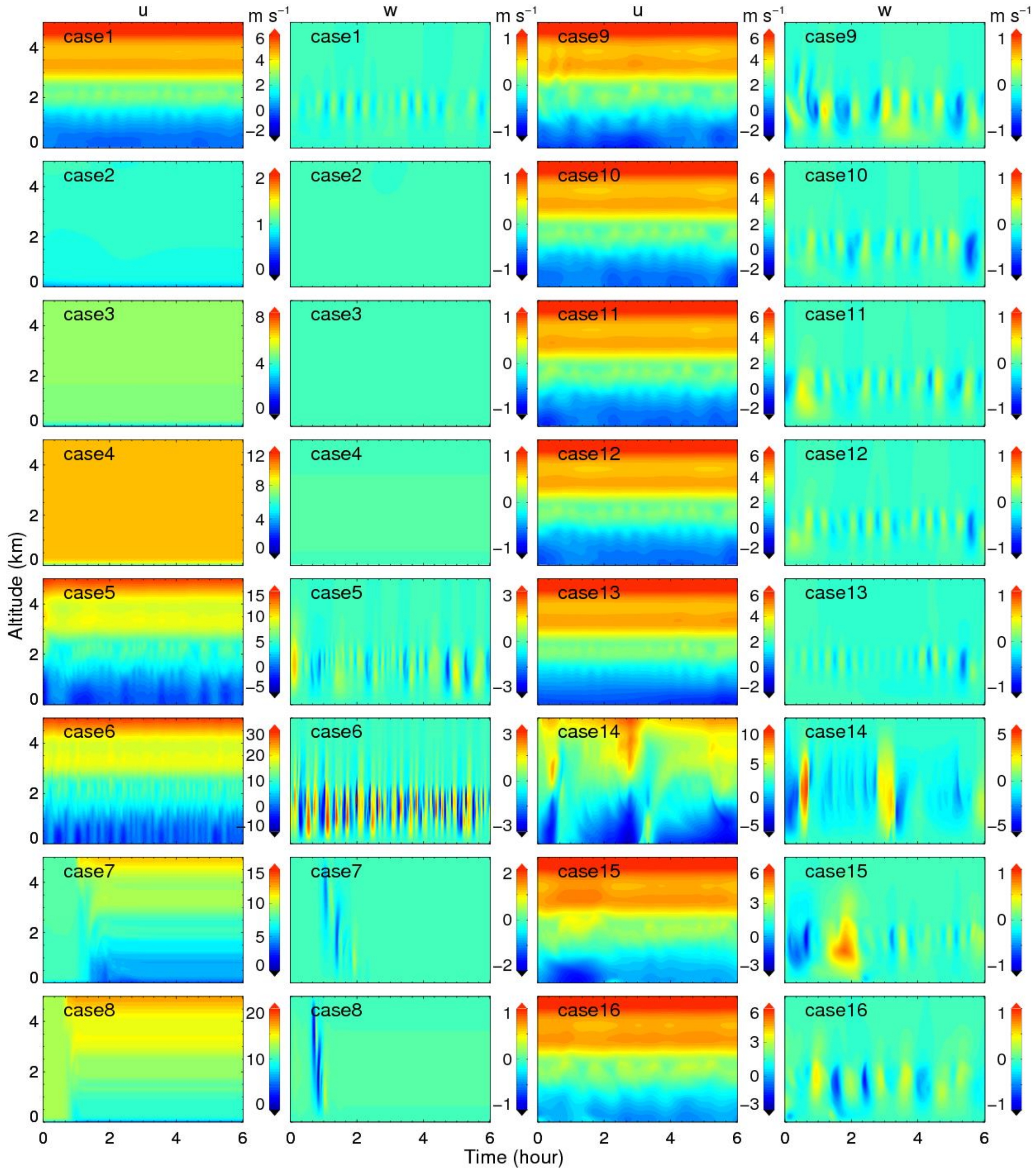

~~**Figure 9.** The simulated zonal wind u and vertical wind w above the lidar for all 16 cases as described in Table 2.~~

In case 1, persistent wave motions are not only exist in the vertical wind, but also in zonal wind near and below the low-level jet around 2 km as shown in Fig. ~~9~~8. It is consistent with lidar detections as shown in Fig. 4. It is obvious that no wave motions are generated with uniform wind speed of 1, 5 and 10 m s^{-1} in ~~case~~cases 2~4. Thus GWs cannot be excited without wind shear here. From the results of case 1, 5 and 6, the wave amplitudes and frequencies increase with the enhancement of wind shears. For case 1, 7 and 8, no persistent wave motions exist with the wind speeds increasing without enhancement of wind shears. Only several solitary wavelike motions can be found when the wind flow passed by the lidar and dissipated rapidly. In addition, the wave motions in case 1~8 are mainly exist under 2.5 km where wind speeds are relatively weak. Therefore, it can be inferred that it is beneficial to the generation of persistent waves under persistent weak wind conditions, which is consistent with previous result in Sect. 3.2.

Table 2. The wind profile and topography for each case in CFD simulations.

Case	Wind profile	Topography	Case	Wind profile	Topography
1	$u_z = u_0$	h_A ×1, h_B ×1	9	$u_z = u_0$	h_A ×0, h_B ×0
2	u_z = 1 m s^{-1}	h_A ×1, h_B ×1	10	$u_z = u_0$	h_A ×0, h_B ×1
3	u_z = 5 m s^{-1}	h_A ×1, h_B ×1	11	$u_z = u_0$	h_A ×1, h_B ×0
4	u_z = 10 m s^{-1}	h_A ×1, h_B ×1	12	$u_z = u_0$	h_A ×2, h_B ×0
5	$u_z = u_0 \times 2$	h_A ×1, h_B ×1	13	$u_z = u_0$	h_A ×4, h_B ×0
6	$u_z = u_0 \times 4$	h_A ×1, h_B ×1	14	$u_z = u_0$	h_A ×6, h_B ×0
7	$u_z = u_0$ + 5 m s^{-1}	h_A ×1, h_B ×1	15	$u_z = u_0$	h_A ×0, h_B ×2
8	$u_z = u_0$ + 10 m s^{-1}	h_A ×1, h_B ×1	16	$u_z = u_0$	h_A ×0, h_B ×4

What will happen when the height of hills A and B near the lidar location are changed? In case 9~11, persistent wave structures still exist with only a few changes when the hills A and/or B disappeared. From case 9 and 11~13, persistent wave structures always exist and do not change significantly. When the height of A increased to h_A ×6 in case 14, i.e., the height of the low-level jet near 2 km altitude, the zonal wind structure changes significantly. In case 9~10 and 15~16, the wave motions also exist and do not change significantly even though the height of B increased to the height of the low-level jet, h_B ×4. Therefore, based on these results of simulation cases, persistent GWs are excited by the persistent wind shear around the low-level jet. The wave structures mainly occur under weak winds. The topography, i.e., the around hills near the station as shown in Fig. 1b, plays a negligible role in the GW generation. Nevertheless, the topography may play a more important role in the downstream when the height of jet is comparable with the height of topography.

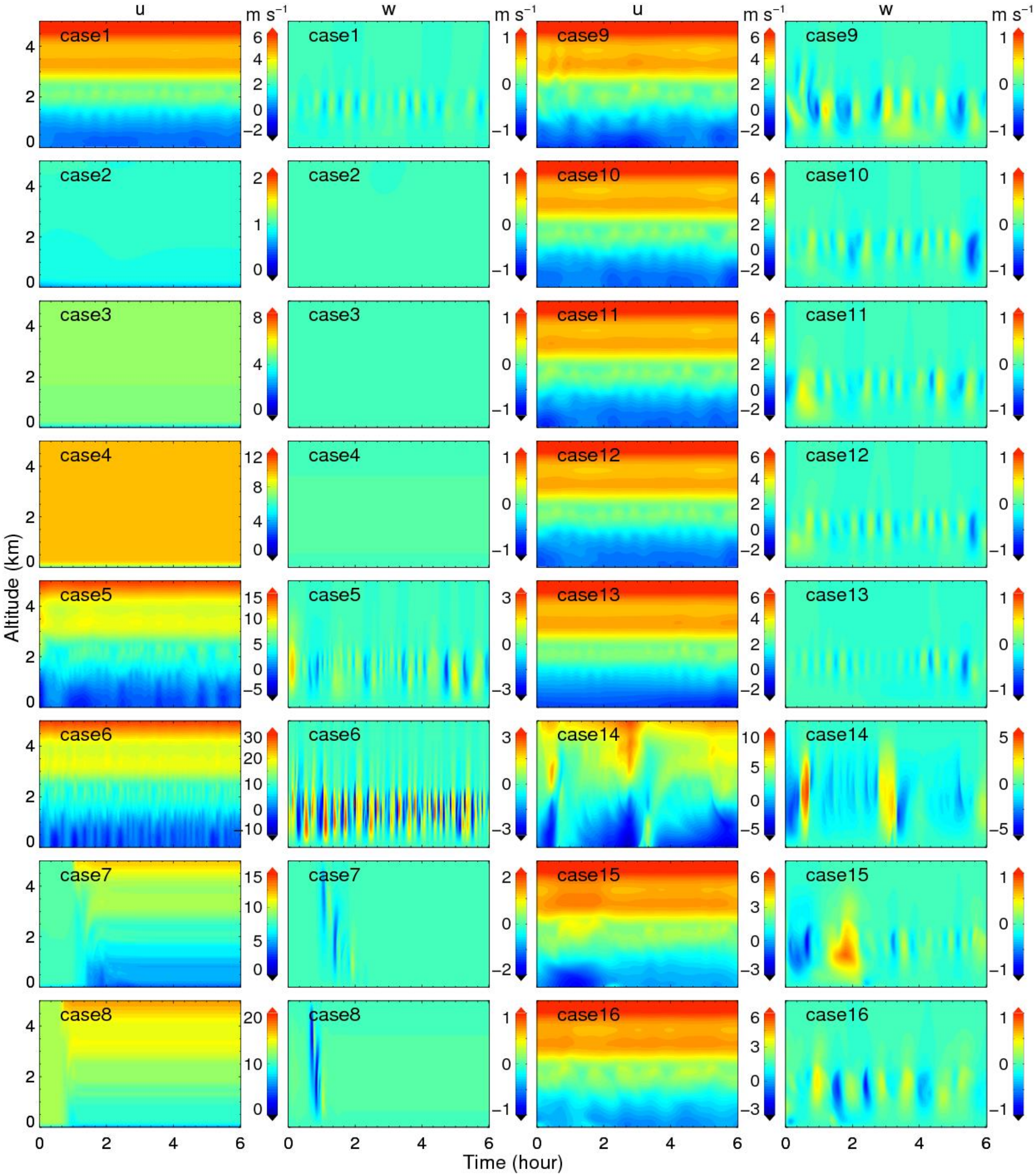

Figure 8. The simulated zonal wind u and vertical wind w above the lidar for all 16 cases as described in Table 2.

5 Discussion

Based on the above experiments and simulations, the mechanism of the persistent wave motions can be inferred as follows. A westerly low-level jet of ~5 m s^{-1} exists above the background southeasterly light wind. The light wind may be in relation to Huangshan and Dabie Mountain. The weak wind shear around the low-level jet may lead to the appearance of wave motions in the light wind. In addition, a strongly stable thermal stratified ABL with inversion layer occurs during the night in Anqing. Negative values of N^2 appear near the altitude of ~2 km. Thereby, the wave motions may be trapped in a ducted structure with long lifetime. The GWs exist without apparent phase progression with altitude in the whole ABL from the surface to the height of ~2 km.

Such quasi monochromatic waves with multi wave cycles and approximately constant period and amplitude are infrequently observed in the ABL (Mahrt, 2014). Nevertheless, similar quasi monochromatic wave motions with multi wave cycles have been reported in several studies. Banakh and Smalikho (2016) revealed a coastal-mountain lee wave with period of ~9 min at daytime on 23 August 2015 in the stable stratified ABL on the coast of Lake Baikal. The wave exists between 100 m and 900 m height range with a lifetime of about 4 h. This wave was suggested to be in relation to the presence of two narrow jet streams at heights of about 200 m and 700 m above ground level. Similar wave motions were also detected in the vertical wind accompanied with a low-level jet in Banakh and Smalikho (2018). It is regrettable that the authors have not given a discussion on the contaminated wavelike motions from 01:00 to 08:00, except the internal wave with period of ~6 min at 07:00. Fritts et al. (2003) reported wave motions with periods typically 4~5 min below the height of ~800 m under light wind with a low-level jet, clear sky conditions throughout the night of 14 October 1999. These wave motions were interpreted as ducted GWs that propagate horizontally along maxima of the stratification and mean wind, and that are evanescent above, and possibly below and/or between, the ducting level(s) (Fritts et al., 2003). Viana et al. (2009) also reported a ducted mesoscale gravity wave over a weakly-stratified nocturnal ABL. This wave lasted less than 10 wave cycles, about 2 hours, with periods of ~16 min. Román-Cascón et al. (2015) analysed non-local GWs generated by wind shear or low-level jet trapped within the stable ABL. With acoustic echo sounder, similar wave motions were also observed without apparent phase progression with altitude in stably stratified ABL several decades ago (Beran et al., 1973; Hooke and Jones, 1986).

The wave motions mentioned above were mainly ~~occurred~~observed in the stable boundary layer under the height of ~1000 m or even ~100 m, while the wave motions exist from surface layer to as high as ~2000 m in our study due to different capability of measurements. ~~In a previous study presented by ,~~In addition, the lifetime of the ducted GWs is more than 10 hours and 20 wave cycles, while in previous studies listed above, most of the lifetimes are less than hours with several wave cycles. These characters make this ducted GWs unique and novel. However, in one of our previous study, obvious wave motions with periods of 10~30 min in vertical wind were observed in the whole residual layer from 1 June 2018 to 2 June 2018 by a similar CDL system (Wang et al., 2019).

The mechanism of this long-~~live~~lived GWs is in consistent with other similar wave motions referenced above in some aspects. Low-level jet or wind shear is one of the mainly sources of such wavelike motions in the ABL. Stably stratified ABL usually leads to effective ducting quasi monochromatic wave motions with a long lifetime and multi wave cycles. Although wind shear near the low-level jet is the main source of GWs as discussed in Sect. 4.2, weaker wind shear is more favorable to the existence of high frequency GWs. Similarly, the surrounding hills play negligible roles in generating the ducted GWs while Dabie Mountain and Huangshan may have an impact on the generation and existence of GWs.

The vertical structure of GWs is describe by Taylor-Goldstein equation (Gossard and Hooke, 1975):

$$m^2 = \frac{N^2}{c_i^2} + \frac{\bar{u}_{zz}}{\mathrm{c_i}} - k_h^2 - \frac{1}{4H^2} \qquad (46)$$

where m is the vertical wavenumber, c_i is the intrinsic phase speed in the direction of propagation, $\bar{u}_{zz}$ is the second derivative with height of the mean wind in the direction of wave propagation, k_h is the horizontal wavenumber, H is the scale height. A sufficiently deep atmospheric layer is required for a wave duct with positive values of m^2. To resolve this equation, the vertical profile of squared buoyancy frequency, which is calculated by temperature profile measured by radiosonde, is shown in Fig. 5b. Simultaneous hourly mean wind, required to resolve c_i and $\bar{u}_{zz}$, can be obtained from lidar measurements. However, the horizontal structures of this wave motion, i.e., c_i and k_h, are still unclear in this study. Horizontal structures of wavelike motions in ABL can be detected by airborne lidar (Chouza et al., 2016; Witschas et al., 2017) and ground-based lidar with range height indicator (RHI) scans (Poulos et al., 2002; Wang, 2013) or plan position indicator (PPI) scans (Mayor, 2017). GW parameters, such as horizontal phase speed, horizontal wavelength, propagation direction, intrinsic frequency, can be resolved from these measurements. Nevertheless, we try to illustrate the character of this ducted wave for a plausible propagation direction and horizontal wavelength from CFD simulations. The propagation direction is assumed to be westerly here as the simulated wave is westerly from the movie in the Supplement. Thus the horizontal wavelength is equal to zonal wavelength which is estimated as ~3 km in Sect. 4.2.

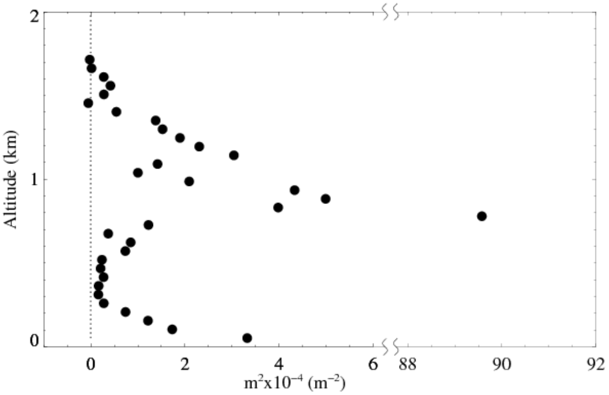

Figure 9. The vertical profile of vertical wave number squared. The dotted line represents zero line.

The vertical profile of vertical wave number squared is shown in Fig. ~~10~~9. The singular point of the relative maxima m^2 in right panel is caused by critical level where the intrinsic frequency is Doppler-shifted close to zero. A ducting process occurs between ~1.5 km altitude and the ground where $m^2 > 0$. It is a result of the combination of thermal and Doppler ducts. The thermal duct is dominant under the temperature inversion with maxima buoyancy frequency squared for all propagation directions as shown in Fig. 5. The Doppler duct is dominant between ~0.5 and ~1.5 km altitude range due to the critical level induced by the low-level jet of wind maximum in a particular direction. Thus the ducted motions give a plausible explanation for the trap of the long-~~live~~lived GW in the ABL.

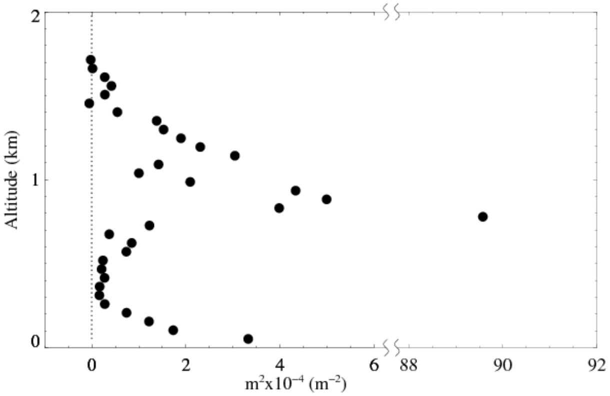

It should be noted that the retrieval of horizontal wind is based on the hypothesis of a homogeneity wind field on a horizontal plane. Accompanying with wave activities, the radius of scanning beams cone will lead to bias on the retrieved horizontal wind. If the radius is equivalently to or larger than the scale of the horizontal wavelength of the GWs, these bias may be significantly affect the result in horizontal component, especially the amplitude of the retrieved GWs. Nevertheless, the bias in the period of the wave motions is negligible. If the radius is smaller than the scale of the horizontal wavelength of the GWs, the bias in both amplitude and period can be ignored. In this study, the horizontal wavelength is estimated as ~3 km in Sect. 4.2. The radius is about 580 m and 870 m at 1 km and 2 km altitude, respectively. Thus, the retrieved bias can be ignored in this study.

More accurate results can be obtained by using three-dimensional (3D) model with accurate boundary conditions when simulating wind flow in complex mountain areas. However, the actual wind field and terrain are complex. It is difficult to obtain accuracy boundary conditions for 3D model. In addition, 3D model consumes much more computing resources and time than 2D model. As a simplification of the actual mountain model, the comparison between numerical simulation results and field experiments shows that the two-dimensional model can simulate the actual topographic flow well (Miller and Davenport, 1998; Toparlar et al., 2017; Walmsley et al., 1984)~~Figure 10. The vertical profile of~~. Some basic theories and empirical formulas of complex mountain wind field are built on the basis of two-dimensional model. Therefore, the two-dimensional terrain simulation of mountain wind field has a wide range of theoretical significance and practicability. By using this simplified 2D model, the influence of terrain on GWs can be still analyzed.

~~vertical wave number squared. The dotted line represents zero line.~~

6 Conclusion

A persistent wave motion was investigated by experiments and numerical simulations. From 4 to 5 in September 2018, GWs with periods of 10~30 min were observed in the whole ABL from ground to the height of ~2 km by a coherent Doppler lidar during a field experiment in Anqing. The amplitudes of these GWs were about 0.15~0.2 m s^{-1} in vertical wind. These GWs existed more than 20 wave cycles. The periods were about 15~25 min before 03:00 LT and 20~30 min after that. A westerly low-level jet was observed at the altitude of 1~2 km in the ABL with maxima speeds of 5~10 m s^{-1}. Simultaneous temperature profiles from radiosonde measurement and ERA5 reanalysis data confirmed the existence of a strong stably stratified ABL. There was an inversion layer under the altitude of ~500 m and negative buoyancy frequency squared near the height of ~2 km. Note that there was no apparent phase progression with altitude of these GWs. Moreover, the vertical and zonal perturbations of the GWs were ~~apparent quadrature~~90 °out of phase with vertical perturbations generally leading zonal perturbations. These characteristics suggested that such GW motions are ducted GWs trapped in the ABL which is also verified by the vertical structure of the wave motions. ~~In addition, the relations between high frequency GWs and background wind conditions were also analysed. High frequency GWs were likely to exist under weak wind and weak wind shear. When the horizontal wind was along the northwest-southeast direction, where Huangshan and Dabie Mountain located, the occurrence rate of such GWs was higher in the ABL.~~ Based on simplified 2-D CFD numerical simulations, the generation mechanisms of such GWs were discussed. The low-level jet streams were considered to be responsible for the excitation of GW motions in present study. Wave motions mainly occurred under weaker wind conditions, which is consistent with ~~previous result and~~ other studies of such ducted waves. The contributions from flow over the surrounding hills could be ignored.

The current study contributes to our understanding of GWs generation mechanism in the ABL, which plays a key role in atmospheric dynamics. Furthermore, the National Meteorological Observing Station of Anqing is close to an airport as shown in Fig. 1b, which will be affected by the clear air turbulence caused by breaking GWs~~.~~ and rotors by the trapped GWs. The application of such coherent Doppler lidar will enhance the measurement capability with high quality data in the ABL, thus enriching our knowledge and improving our abilities in aviation safety, weather forecast and climate models in future. However, the horizontal structures of the GWs are still unclear in this study. Simultaneous measurements with multi lidars and multi scanning modes are required in further studies.

Data availability

The ERA5 data sets are publicly available from ECMWF website at https://www.ecmwf.int/en/forecasts/datasets/reanalysis-datasets/era5, last access: 1 March 2019. The elevation data are available at SRTM website (http://srtm.csi.cgiar.org, last access: 1 March 2019). Lidar and radiosonde data can be downloaded from http://www.lidar.cn/datashare/Jia_et_al_2019.rar, last access: 16 March 2019.

Appendix A: Lidar observational results during the experiment

The vertical wind, horizontal wind speed, wind direction and CNR during the field experiment from 16 August to 5 September 2018 are shown in Fig. A1~A4, respectively.

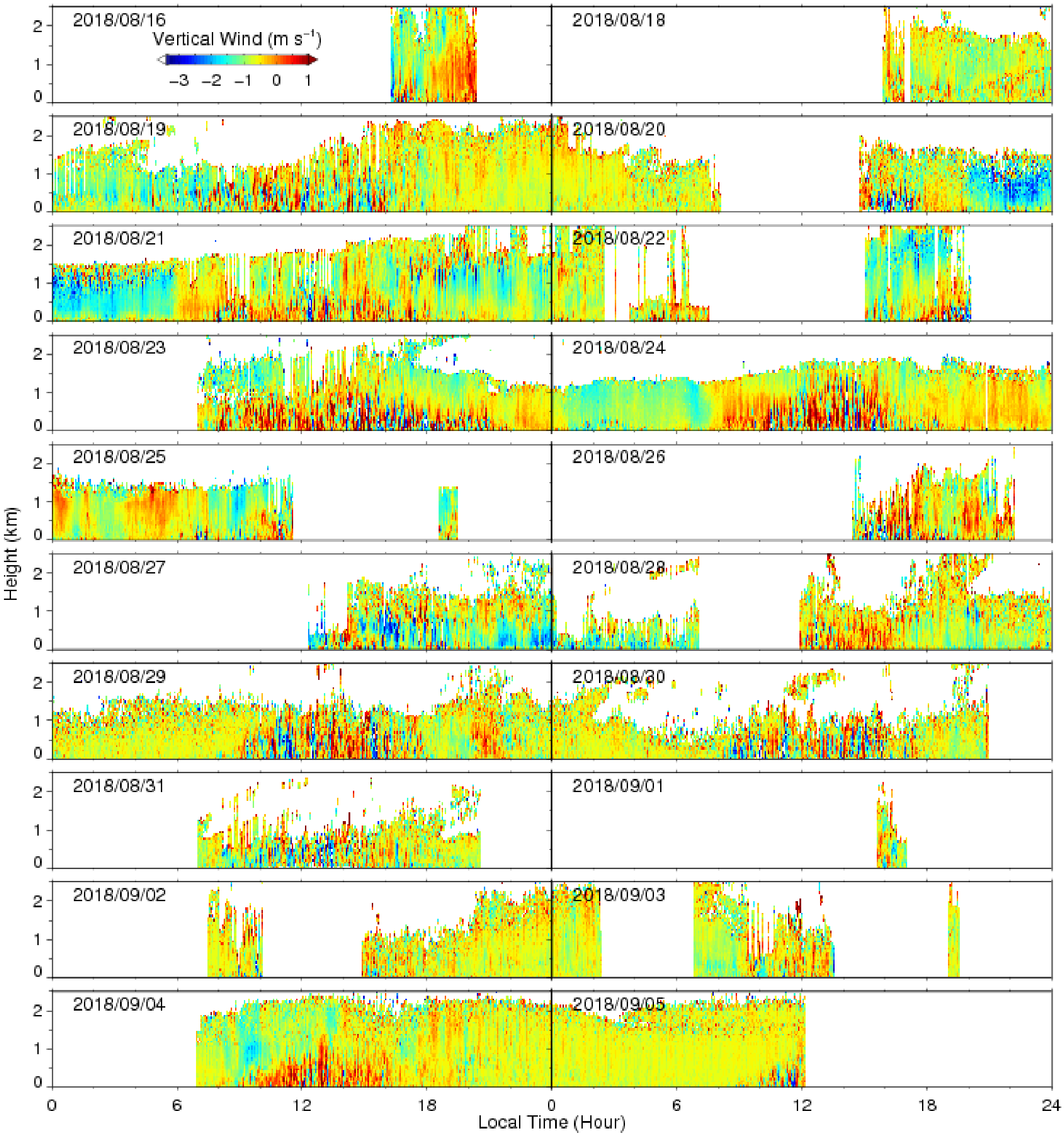

5 **Figure A1.** Time height cross section of vertical wind speed per day during the experiment. Dates are shown in the top left of each panel, and are read as YYYY/MM/DD.

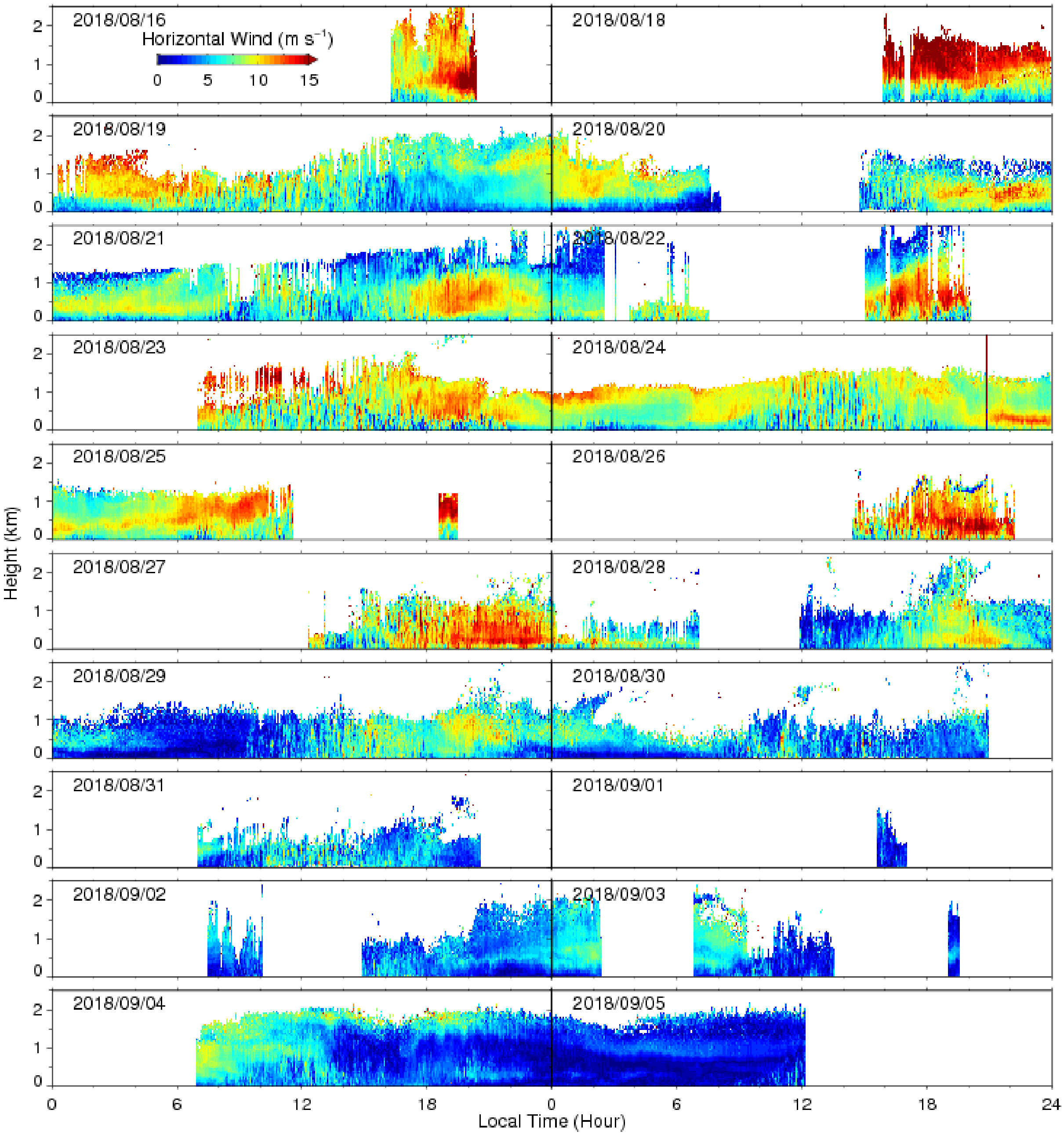

Figure A2. Similar to Fig. A1 but for horizontal wind speed**.**

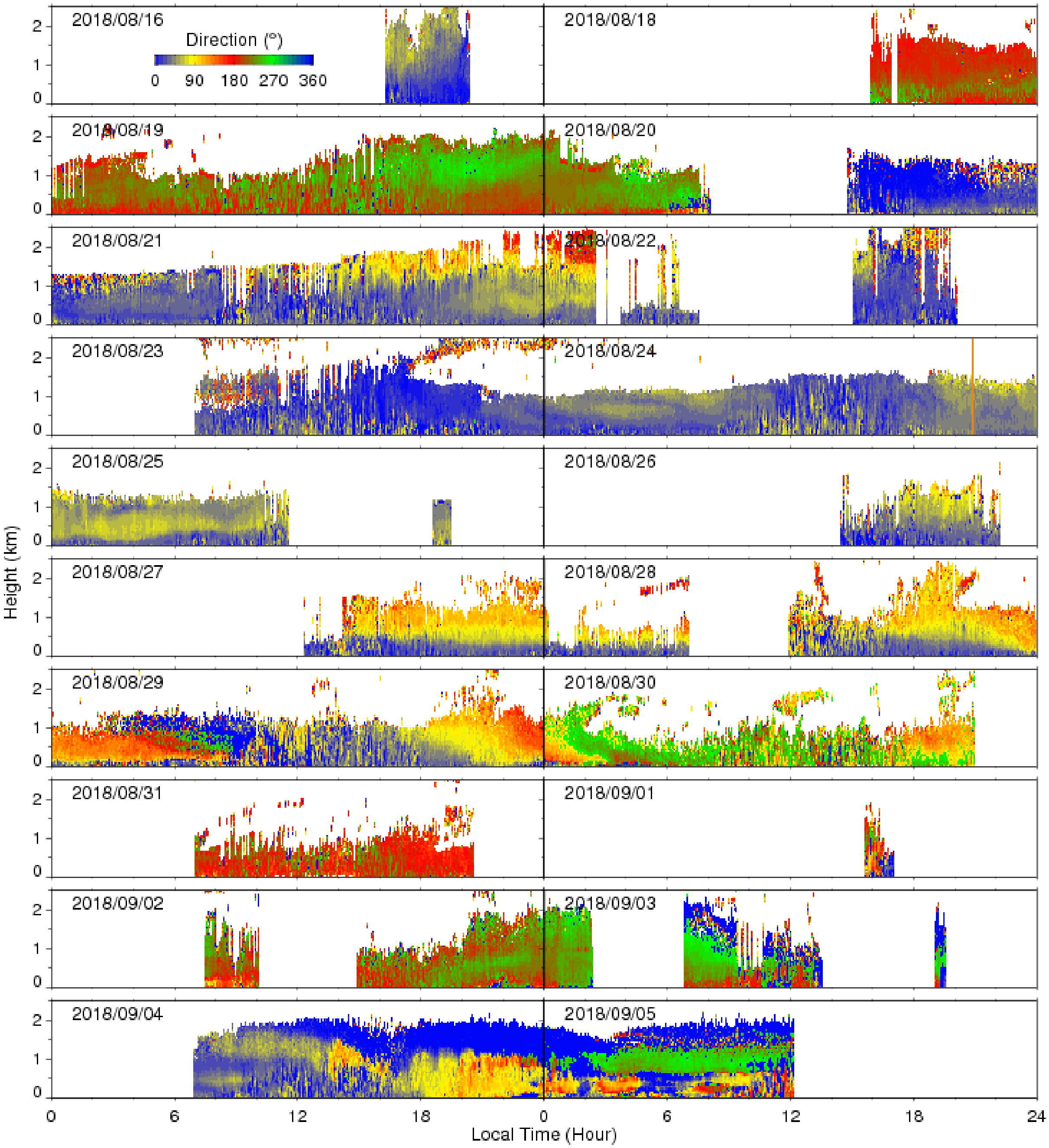

Figure A3. Similar to Fig. A1 but for horizontal wind direction.

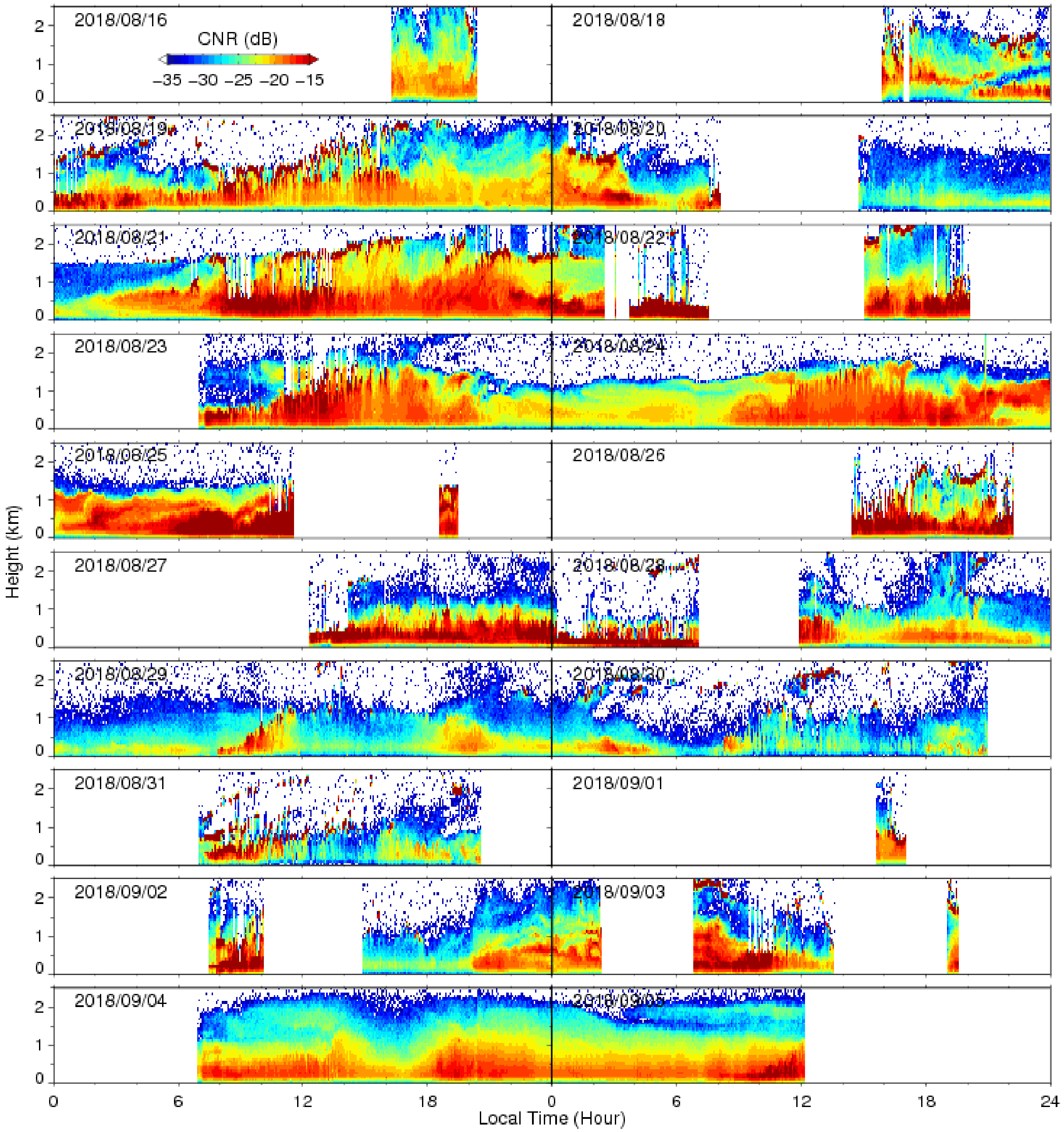

Figure A4. Similar to Fig. A1 but for CNR.

~~Appendix B: Identification of dominant high frequency GWs~~

~~In order to extract high frequency GWs with periods of 5~50 min, a window of 4-hour length and 200-m height shifted in steps of 1 hour temporally and 100 m vertically is used. First, height averaged temporal profiles are obtained in a given window,~~

~~such as vertical wind in Fig. B1a and B1b. Second, the corresponding Morlet wavelet power spectrum and Lomb–Scargle (LS) periodogram are calculated as shown in Fig. B1b~1f. Significance levels of LS and wavelet are used to identify GWs. Period ranges of 5~50 min are indicated by the vertical dotted lines in Fig. B1e and B1f. Thirdly, maxima values in LS spectral larger than significance level within periods of 5~50 min are identified as the potential waves W1 as shown in Fig. B1e and B1f. Then, the average of wavelet significance in the central 1-hour areas, between the skyblue dashed lines in Fig. B1c and B1d, are plotted as the brown dash dotted lines as shown in Fig. B1e and B1f. Potential waves W2 are also identified by the significance levels. Following this, the potential waves W1 and W2 are compared. W1 and W2 with maximum amplitudes and relative differences in periods less than 30% are considered to be the best matched pairs. For example, W1 and W2 are well matched in Fig. B1e while are not matched in Fig. B1f. Finally, these matched pairs of potential waves are identified as the dominant GWs in a specified window. If no W1 or W2 are recognized, or no pairs of W1 and W2 are matched, it skips to the next temporal-spatial window. Thus we can know whether there is a dominant high frequency wave motion in a specified temporal-spatial window or not.~~

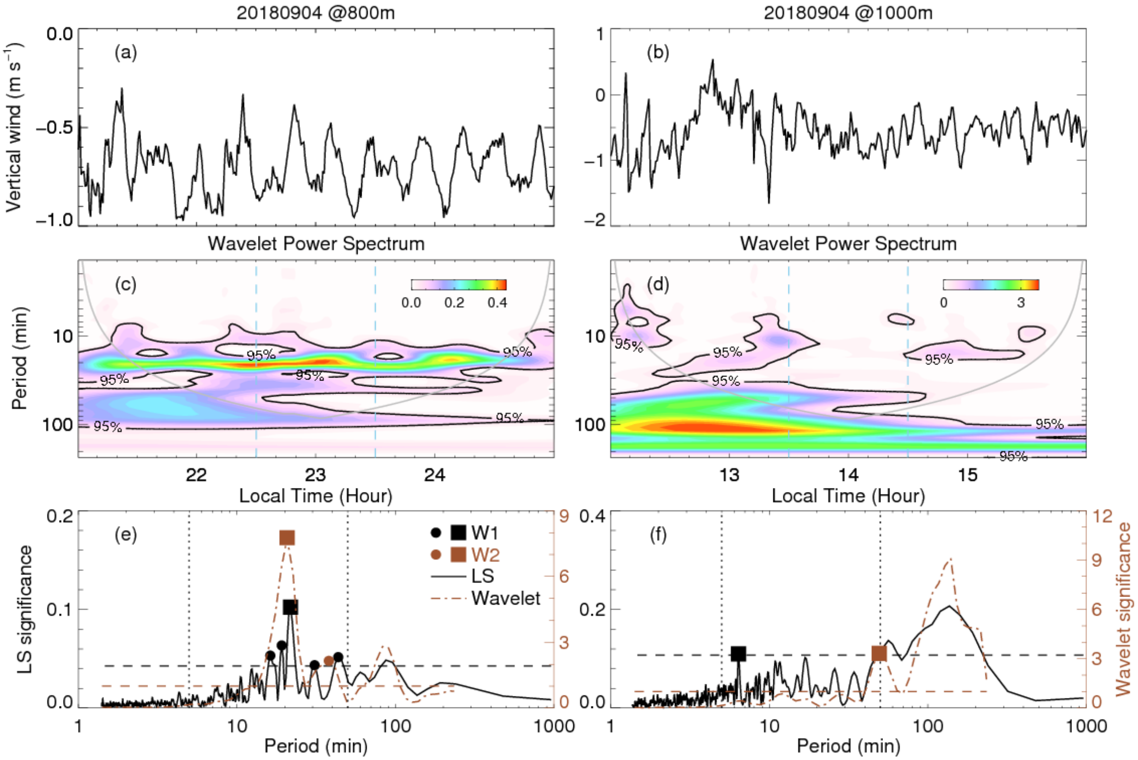

~~**Figure B1.** (a) Average temporal vertical wind in a given window. (c) Morlet wavelet power spectrum of vertical wind. The black contours indicate significance level of 95%. The gray line represent the Corn-of-Influence (COI). The skyblue vertical dashed lines indicate the central one hour area of the temporal window. (e) LS periodograms of the vertical wind (black solid line). Average signicance between the skyblue dashed lines in (c) (brown dash dotted line). The black vertical dotted lines represent period range of 5~50 min as high frequency waves. Black and brown dashed lines indicate the significance levels of LS periodograms and wavelet, respectively. The black solid circles represent potential waves W1, while the brown represent potential W2. Solid squares indicate the identified waves. (b)(d)(f) are same as (a)(c)(e) but in a different temporal-spatial window.~~

~~However, we note that such a simple and rough method may result in unrealistic wave signals due to the false detection. During the START08 field experiment, confirmed that part of the wavelike motions may be due to intrinsic observational errors or other physical phenomena (e.g., nonlinear dynamics, shear instability and/or turbulence). Nevertheless, the relation between high frequency GWs and weak wind is consistent with CFD numerical simulations in Sect. 4 and previous studies referenced in Sect. 5. Thus the methodology of dominant GW identification is still reasonable in this manuscript.~~

Author contribution

HX conceived, designed the study. YW, LZ CW and MJ performed the lidar experiments. MJ, CW and TW performed the lidar data analysis. LL, DL and RC provide the field experiment site and the radiosonde data. JW analyzed ERA5 data. JY performed the CFD numerical simulations. MJ and JY carried out the analysis and prepared the figures, with comments from other co-authors. MJ, HX, XX and XD interpreted the data. MJ, JY and HX wrote the manuscript. All authors read and approved the final manuscript.

Competing interests.

The authors declare that they have no conflict of interest.

Acknowledgements.

We acknowledge the use of ERA5 data sets from ECMWF website at https://www.ecmwf.int/en/forecasts/datasets/ reanalysis-datasets/era5. We acknowledge the use of elevation data sets from SRTM website at http://srtm.csi.cgiar.org.

References

Banakh, V., and Smalikho, I.: Lidar Studies of Wind Turbulence in the Stable Atmospheric Boundary Layer, Remote Sensing, 10, 1219, 10.3390/rs10081219, 2018.

Banakh, V. A., and Smalikho, I. N.: Lidar observations of atmospheric internal waves in the boundary layer of the atmosphere on the coast of Lake Baikal, Atmospheric Measurement Techniques, 9, 5239-5248, 10.5194/amt-9-5239-2016, 2016.

Beran, D. W., Hooke, W. H., and Clifford, S. F.: Acoustic echo-sounding techniques and their application to gravity-wave, turbulence, and stability studies, Boundary-Layer Meteorology, 4, 133-153, 10.1007/bf02265228, 1973.

Berg, J., Troldborg, N., Sørensen, N. N., Patton, E. G., and Sullivan, P. P.: Large-Eddy Simulation of turbine wake in complex terrain, Journal of Physics: Conference Series, 854, 012003, 10.1088/1742-6596/854/1/012003, 2017.

Bian, J., Chen, H., Vömel, H., Duan, Y., Xuan, Y., and Lü, D.: Intercomparison of humidity and temperature sensors: GTS1, Vaisala RS80, and CFH, Advances in Atmospheric Sciences, 28, 139-146, 10.1007/s00376-010-9170-8, 2010.

Birch, C. E., Parker, D. J., O'Leary, A., Marsham, J. H., Taylor, C. M., Harris, P. P., and Lister, G. M. S.: Impact of soil moisture and convectively generated waves on the initiation of a West African mesoscale convective system, Quarterly Journal of the Royal Meteorological Society, 139, 1712-1730, 10.1002/qj.2062, 2013.

Blumen, W., Banta, R. M., Berri, G., Blumen, W., Carruthers, D. J., Dalu, G. A., Durran, D. R., Egger, J., Garratt, J. R., Hanna, S. R., Hunt, J. C. R., Meroney, R. N., Miller, W., Neff, W. D., Nicolini, M., Paegle, J., Pielke, R. A., Smith, R. B., Strimaitis, D. G., Vukicevic, T., and Whiteman, C. D.: Atmospheric Processes over Complex Terrain, Meteorological Monographs, 57, American Meteorological Society, Boston, MA, 1990.

Chouza, F., Reitebuch, O., Jähn, M., Rahm, S., and Weinzierl, B.: Vertical wind retrieved by airborne lidar and analysis of island induced gravity waves in combination with numerical models and in situ particle measurements, Atmospheric Chemistry and Physics, 16, 4675-4692, 10.5194/acp-16-4675-2016, 2016.

Clark, T. L., Hall, W. D., Kerr, R. M., Middleton, D., Radke, L., Ralph, F. M., Neiman, P. J., and Levinson, D.: Origins of aircraft-damaging clear-air turbulence during the 9 December 1992 Colorado downslope windstorm: Numerical simulations and comparison with observations, Journal of the Atmospheric Sciences, 57, 1105-1131, Doi 10.1175/1520-0469(2000)057<1105:Ooadca>2.0.Co;2, 2000.

Cohn, S. A., Holloway, C. L., Oncley, S. P., Doviak, R. J., and Lataitis, R. J.: Validation of a UHF spaced antenna wind profiler for high-resolution boundary layer observations, Radio Science, 32, 1279-1296, 10.1029/97rs00578, 1997.

Cohn, S. A., Brown, W. O. J., Martin, C. L., Susedik, M. E., Maclean, G. D., and Parsons, D. B.: Clear air boundary layer spaced antenna wind measurement with the Multiple Antenna Profiler (MAPR), Annales Geophysicae, 19, 845-854, 10.5194/angeo-19-845-2001, 2001.

Corby, G. A.: A preliminary study of atmospheric waves using radiosonde data, Quarterly Journal of the Royal Meteorological Society, 83, 49-60, 10.1002/qj.49708335505, 1957.

Einaudi, F., and Finnigan, J. J.: The interaction between an internal gravity wave and the planetary boundary layer. Part I: The linear analysis, Quarterly Journal of the Royal Meteorological Society, 107, 793-806, 10.1002/qj.49710745404, 1981.

El Kasmi, A., and Masson, C.: Turbulence modeling of atmospheric boundary layer flow over complex terrain: a comparison of models at wind tunnel and full scale, Wind Energy, 13, 689-704, 10.1002/we.390, 2010.

Fernando, H. J. S., Mann, J., Palma, J. M. L. M., Lundquist, J. K., Barthelmie, R. J., BeloPereira, M., Brown, W. O. J., Chow, F. K., Gerz, T., Hocut, C. M., Klein, P. M., Leo, L. S., Matos, J. C., Oncley, S. P., Pryor, S. C., Bariteau, L., Bell, T. M., Bodini, N., Carney, M. B., Courtney, M. S., Creegan, E. D., Dimitrova, R., Gomes, S., Hagen, M., Hyde, J. O., Kigle, S., Krishnamurthy, R., Lopes, J. C., Mazzaro, L., Neher, J. M. T., Menke, R., Murphy, P., Oswald, L., Otarola-Bustos, S., Pattantyus, A. K., Rodrigues, C. V., Schady, A., Sirin, N., Spuler, S., Svensson, E., Tomaszewski, J., Turner, D. D., van Veen, L., Vasiljević, N., Vassallo, D., Voss, S., Wildmann, N., and Wang, Y.: The Perdigão: Peering into Microscale Details of Mountain Winds, Bulletin of the American Meteorological Society, 10.1175/bams-d-17-0227.1, 2018.

Finnigan, J. J., and Einaudi, F.: The interaction between an internal gravity wave and the planetary boundary layer. Part II: Effect of the wave on the turbulence structure, Quarterly Journal of the Royal Meteorological Society, 107, 807-832, 10.1002/qj.49710745405, 1981.

Fritts, D. C., and Alexander, M. J.: Gravity wave dynamics and effects in the middle atmosphere, Reviews of Geophysics, 41, 10.1029/2001rg000106, 2003.

Fritts, D. C., Nappo, C., Riggin, D. M., Balsley, B. B., Eichinger, W. E., and Newsom, R. K.: Analysis of Ducted Motions in the Stable Nocturnal Boundary Layer during CASES-99, Journal of the Atmospheric Sciences, 60, 2450-2472, 10.1175/1520-0469(2003)060<2450:aodmit>2.0.co;2, 2003.

Gossard, E. E., and Hooke, W. H.: Waves in the atmosphere: atmospheric infrasound and gravity waves-their generation and propagation, Atmospheric Science, Developments in Atmospheric Science, No. 2, Elsevier Scientific Publishing Co., Amsterdam, 1975.

Grubišić, V., Doyle, J. D., Kuettner, J., Mobbs, S., Smith, R. B., Whiteman, C. D., Dirks, R., Czyzyk, S., Cohn, S. A., Vosper, S., Weissmann, M., Haimov, S., De Wekker, S. F. J., Pan, L. L., and Chow, F. K.: The Terrain-Induced Rotor Experiment, Bulletin of the American Meteorological Society, 89, 1513-1534, 10.1175/2008bams2487.1, 2008.

Holton, J. R., and Alexander, M. J.: The role of waves in the transport circulation of the middle atmosphere, in: Atmospheric Science Across the Stratopause, edited by: Siskind, D. E., Eckermann, S. D., and Summers, M. E., Geophysical Monograph Series, 21-35, 2000.

Hooke, W. H., and Jones, R. M.: Dissipative Waves Excited by Gravity-Wave Encounters with the Stably Stratified Planetary Boundary Layer, Journal of the Atmospheric Sciences, 43, 2048-2060, 10.1175/1520-0469(1986)043<2048:dwebgw>2.0.co;2, 1986.

Kuettner, J. P., Hildebrand, P. A., and Clark, T. L.: Convection waves: Observations of gravity wave systems over convectively active boundary layers, Quarterly Journal of the Royal Meteorological Society, 113, 445-467, 10.1002/qj.49711347603, 2007.

Lac, C., Lafore, J. P., and Redelsperger, J. L.: Role of gravity waves in triggering deep convection during TOGA COARE, Journal of the Atmospheric Sciences, 59, 1293-1316, Doi 10.1175/1520-0469(2002)059<1293:Rogwit>2.0.Co;2, 2002.

Lapworth, A., and Osborne, S. R.: Evidence for gravity wave drag in the boundary layer of a numerical forecast model: a comparison with observations, Quarterly Journal of the Royal Meteorological Society, 142, 3257-3264, 10.1002/qj.2909, 2016.

Li, F.: New developments with upper-air sounding in China, WMO, Instruments and Observing Methods Report 94, Geneva, Switzerland, 2006.

Lyulyukin, V. S., Kallistratova, M. A., Kouznetsov, R. D., Kuznetsov, D. D., Chunchuzov, I. P., and Chirokova, G. Y.: Internal gravity-shear waves in the atmospheric boundary layer from acoustic remote sensing data, Izvestiya, Atmospheric and Oceanic Physics, 51, 193-202, 10.1134/s0001433815020103, 2015.

Mahrt, L.: Stably Stratified Atmospheric Boundary Layers, Annual Review of Fluid Mechanics, 46, 23-45, 10.1146/annurev-fluid-010313-141354, 2014.

Mann, J., Angelou, N., Arnqvist, J., Callies, D., Cantero, E., Arroyo, R. C., Courtney, M., Cuxart, J., Dellwik, E., Gottschall, J., Ivanell, S., Kuhn, P., Lea, G., Matos, J. C., Palma, J. M., Pauscher, L., Pena, A., Rodrigo, J. S., Soderberg, S., Vasiljevic, N., and Rodrigues, C. V.: Complex terrain experiments in the New European Wind Atlas, Philosophical transactions. Series A, Mathematical, physical, and engineering sciences, 375, 10.1098/rsta.2016.0101, 2017.

Marsham, J. H., and Parker, D. J.: Secondary initiation of multiple bands of cumulonimbus over southern Britain. II: Dynamics of secondary initiation, Quarterly Journal of the Royal Meteorological Society, 132, 1053-1072, 10.1256/qj.05.152, 2006.

Mayor, S. D.: Observations of microscale internal gravity waves in very stable atmospheric boundary layers over an orchard canopy, Agr Forest Meteorol, 244, 136-150, 10.1016/j.agrformet.2017.05.014, 2017.

Miller, C. A., and Davenport, A. G.: Guidelines for the calculation of wind speed-ups in complex terrain, Journal of Wind Engineering and Industrial Aerodynamics, 74-76, 189-197, 10.1016/s0167-6105(98)00016-6, 1998.

Neiman, P. J., Hardesty, R. M., Shapiro, M. A., and Cupp, R. E.: Doppler Lidar Observations of a Downslope Windstorm, Monthly Weather Review, 116, 2265-2275, 10.1175/1520-0493(1988)116<2265:dlooad>2.0.co;2, 1988.

Newsom, R. K., and Banta, R. M.: Shear-Flow Instability in the Stable Nocturnal Boundary Layer as Observed by Doppler Lidar during CASES-99, Journal of the Atmospheric Sciences, 60, 16-33, 10.1175/1520-0469(2003)060<0016:sfiits>2.0.co;2, 2003.

Plougonven, R., and Zhang, F.: Internal gravity waves from atmospheric jets and fronts, Reviews of Geophysics, 52, 33-76, 10.1002/2012rg000419, 2014.

Poulos, G. S., Blumen, W., Fritts, D. C., Lundquist, J. K., Sun, J., Burns, S. P., Nappo, C., Banta, R., Newsom, R., Cuxart, J., Terradellas, E., Balsley, B., and Jensen, M.: CASES-99: A Comprehensive Investigation of the Stable Nocturnal Boundary Layer, Bulletin of the American Meteorological Society, 83, 555-581, 10.1175/1520-0477(2002)083<0555:caciot>2.3.co;2, 2002.

Pramitha, M., Venkat Ratnam, M., Taori, A., Krishna Murthy, B. V., Pallamraju, D., and Vijaya Bhaskar Rao, S.: Evidence for tropospheric wind shear excitation of high-phase-speed gravity waves reaching the mesosphere using the ray-tracing technique, Atmospheric Chemistry and Physics, 15, 2709-2721, 10.5194/acp-15-2709-2015, 2015.

Preusse, P., Ern, M., Bechtold, P., Eckermann, S. D., Kalisch, S., Trinh, Q. T., and Riese, M.: Characteristics of gravity waves resolved by ECMWF, Atmospheric Chemistry and Physics, 14, 10483-10508, 10.5194/acp-14-10483-2014, 2014.

Ren, H., Laima, S., Chen, W.-L., Zhang, B., Guo, A., and Li, H.: Numerical simulation and prediction of spatial wind field under complex terrain, Journal of Wind Engineering and Industrial Aerodynamics, 180, 49-65, 2018.

Román-Cascón, C., Yagüe, C., Mahrt, L., Sastre, M., Steeneveld, G. J., Pardyjak, E., van de Boer, A., and Hartogensis, O.: Interactions among drainage flows, gravity waves and turbulence: a BLLAST case study, Atmospheric Chemistry and Physics, 15, 9031-9047, 10.5194/acp-15-9031-2015, 2015.

Sun, J., Mahrt, L., Nappo, C., and Lenschow, D. H.: Wind and Temperature Oscillations Generated by Wave–Turbulence Interactions in the Stably Stratified Boundary Layer, Journal of the Atmospheric Sciences, 72, 1484-1503, 10.1175/jas-d-14-0129.1, 2015a.

Sun, J., Nappo, C. J., Mahrt, L., Belušić, D., Grisogono, B., Stauffer, D. R., Pulido, M., Staquet, C., Jiang, Q., Pouquet, A., Yagüe, C., Galperin, B., Smith, R. B., Finnigan, J. J., Mayor, S. D., Svensson, G., Grachev, A. A., and Neff, W. D.: Review of wave-turbulence interactions in the stable atmospheric boundary layer, Reviews of Geophysics, 53, 956-993, 10.1002/2015rg000487, 2015b.

Sun, J. L., Lenschow, D. H., Burns, S. P., Banta, R. M., Newsom, R. K., Coulter, R., Frasier, S., Ince, T., Nappo, C., Balsley, B. B., Jensen, M., Mahrt, L., Miller, D., and Skelly, B.: Atmospheric disturbances that generate intermittent turbulence in nocturnal boundary layers, Boundary-Layer Meteorology, 110, 255-279, Doi 10.1023/A:1026097926169, 2004.

Toms, B. A., Tomaszewski, J. M., Turner, D. D., and Koch, S. E.: Analysis of a Lower-Tropospheric Gravity Wave Train Using Direct and Remote Sensing Measurement Systems, Monthly Weather Review, 145, 2791-2812, 10.1175/mwr-d-16-0216.1, 2017.

Toparlar, Y., Blocken, B., Vos, P., van Heijst, G. J. F., Janssen, W. D., van Hooff, T., Montazeri, H., and Timmermans, H. J. P.: CFD simulation and validation of urban microclimate: A case study for Bergpolder Zuid, Rotterdam, Building and Environment, 83, 79-90, 10.1016/j.buildenv.2014.08.004, 2015.

Toparlar, Y., Blocken, B., Maiheu, B., and van Heijst, G. J. F.: A review on the CFD analysis of urban microclimate, Renewable and Sustainable Energy Reviews, 80, 1613-1640, 10.1016/j.rser.2017.05.248, 2017.

Tsiringakis, A., Steeneveld, G. J., and Holtslag, A. A. M.: Small-scale orographic gravity wave drag in stable boundary layers and its impact on synoptic systems and near-surface meteorology, Quarterly Journal of the Royal Meteorological Society, 143, 1504-1516, 10.1002/qj.3021, 2017.

Vasiljević, N., L. M. Palma, J. M., Angelou, N., Carlos Matos, J., Menke, R., Lea, G., Mann, J., Courtney, M., Frölen Ribeiro, L., and M. G. C. Gomes, V. M.: Perdigão 2015: methodology for atmospheric multi-Doppler lidar experiments, Atmospheric Measurement Techniques, 10, 3463-3483, 10.5194/amt-10-3463-2017, 2017.

Viana, S., Yagüe, C., and Maqueda, G.: Propagation and Effects of a Mesoscale Gravity Wave Over a Weakly-Stratified Nocturnal Boundary Layer During the SABLES2006 Field Campaign, Boundary-Layer Meteorology, 133, 165-188, 10.1007/s10546-009-9420-4, 2009.

Walmsley, J. L., Taylor, P. A., and Salmon, J. R.: Simple guidelines for estimating windspeed variations due to small-scale topographic features–an update, Climatological bulletin, 23, 3-14, 1984.

Wang, C., Xia, H., Shangguan, M., Wu, Y., Wang, L., Zhao, L., Qiu, J., and Zhang, R.: 1.5 μm polarization coherent lidar incorporating time-division multiplexing, Optics express, 25, 20663-20674, 10.1364/OE.25.020663, 2017.

Wang, C., Jia, M., Xia, H., Wu, Y., Wei, T., Shang, X., Yang, C., Xue, X., and Dou, X.: Relationship Analysis of $PM_{2.5}$ and BLH using Aerosol and Turbulence Detection Lidar, Atmospheric Measurement Techniques Discussions, 1-16, 10.5194/amt-2018-406, 2019.

Wang, Y.: Investigation of nocturnal low-level jet–generated gravity waves over Oklahoma City during morning boundary layer transition period using Doppler wind lidar data, Journal of Applied Remote Sensing, 7, 073487, 10.1117/1.jrs.7.073487, 2013.

Watt, S. F. L., Gilbert, J. S., Folch, A., Phillips, J. C., and Cai, X. M.: An example of enhanced tephra deposition driven by topographically induced atmospheric turbulence, Bulletin of Volcanology, 77, 10.1007/s00445-015-0927-x, 2015.

Witschas, B., Rahm, S., Dörnbrack, A., Wagner, J., and Rapp, M.: Airborne Wind Lidar Measurements of Vertical and Horizontal Winds for the Investigation of Orographically Induced Gravity Waves, Journal of Atmospheric and Oceanic Technology, 34, 1371-1386, 10.1175/jtech-d-17-0021.1, 2017.

Wu, J. F., Xue, X. H., Liu, H. L., Dou, X. K., and Chen, T. D.: Assessment of the Simulation of Gravity Waves Generation by a Tropical Cyclone in the High-Resolution WACCM and the WRF, Journal of Advances in Modeling Earth Systems, 10, 2214-2227, 10.1029/2018ms001314, 2018.

Yakhot, V., Orszag, S., Thangam, S., Gatski, T., and Speziale, C.: Development of turbulence models for shear flows by a double expansion technique, Physics of Fluids A: Fluid Dynamics, 4, 1510-1520, 1992.

Yan, B. W., Li, Q. S., He, Y. C., and Chan, P. W.: RANS simulation of neutral atmospheric boundary layer flows over complex terrain by proper imposition of boundary conditions and modification on the k-ε model, Environmental Fluid Mechanics, 16, 1-23, 10.1007/s10652-015-9408-1, 2015.